

Review

Silicon Photonic Biosensors Using Label-Free Detection

Enxiao Luan ^{1,*} , Hossam Shoman ¹, Daniel M. Ratner ², Karen C. Cheung ¹ and Lukas Chrostowski ¹

¹ Department of Electrical and Computer Engineering, University of British Columbia, 2329 West Mall, Vancouver, BC V6T 1Z4, Canada; hoshoman@ece.ubc.ca (H.S.); kcheung@ece.ubc.ca (K.C.C.); lukasc@ece.ubc.ca (L.C.)

² Department of Bioengineering, University of Washington, 3720 15th Ave NE, Seattle, WA 98195-5061, USA; dratner@uw.edu (D.M.R.)

* Correspondence: eluan@ece.ubc.ca; Tel.: +1-778-952-8807

Abstract: Thanks to advanced semiconductor microfabrication technology, chip-scale integration and miniaturization of lab-on-a-chip components, silicon-based optical biosensors have made significant progress for the purpose of point-of-care diagnosis. In this review, we provide an overview of the state-of-the-art in evanescent field biosensing technologies including interferometer, microcavity, photonic crystal, and Bragg grating waveguide-based sensors. Their sensing mechanisms and sensor performances, as well as real biomarkers for label-free detection, are exhibited and compared. We also review the development of chip-level integration for lab-on-a-chip photonic sensing platforms, which consist of the optical sensing device, flow delivery system, optical input and readout equipment. At last, some advanced system-level CMOS-chip packaging examples are presented, indicating the commercialization potential for the low cost, high yield, portable biosensing platform leveraging CMOS processes.

Keywords: silicon photonics, evanescent optical field sensor, label-free SOI biosensor, Mach-Zehnder interferometer, ring resonator, photonic crystal, Bragg grating, sub-wavelength grating, lab-on-a-chip, microfluidics

1. Introduction

Medical diagnostics have come to play a critical role in healthcare by providing early detection and diagnosis of disease [1], improving timely and appropriate care [2], protecting the safety of medical products such as blood for transfusion [3], and reducing healthcare costs [4]. Most diagnostic systems have been designed to meet the requirements of well-funded clinical laboratories in highly regulated environments, but do not address the need of the majority of patients and caretakers in the developing world with inadequate healthcare facilities and clinical laboratories [5]. For instance, the enzyme-linked immunosorbent assay (ELISA), which has been the gold-standard method in biomarker detection and validated for more than 40 years, can obtain an ultra-low detection limit (~ 1 pM) [6]. However, this method is based on a label-based approach which delays results, adds to costs due to specialized reagent requirements, and needs complex micro-evaluations using large, automated analyzers. Therefore, highly sensitive, fast and economic techniques of analysis are desired for both developing and developed countries for point-of-care (POC) diagnostic applications to improve access to cost-effective healthcare technologies.

The development of practical biosensors is one of the most promising approaches to satisfy the growing demand for effective medical diagnostic technologies [7]. Since the first oxygen electrode biosensor demonstrated by Clark in 1956 [8], scientists and engineers have made significant progress in the field of biosensing techniques, which has subsequently been adopted into clinical practice. By 2020, the global biosensors market size is anticipated to reach USD 21.17 billion, among which optical biosensors are identified as the most lucrative technology segment [9]. This represents just a fraction of the estimated USD 72 billion worldwide markets for in vitro diagnostics (IVD). There are a variety of techniques that have been successfully employed for optical measurements, such as emission, absorption, fluorescence, refractometry, and polarimetry [10]. Evanescent field detection is the primary detection principle of many optical biosensors [10]. Due to the sensitivity to changes in the local refractive index (RI) within the evanescent field surrounding the device, evanescent field biosensors such as Surface Plasmon Resonance (SPR) or planar

38 waveguide based sensors have attracted growing interest for sensitive, real-time, and label-free biomolecular
39 detection [11].

40 Several technologies are available for the fabrication of photonic biosensors, and the well-developed
41 silicon photonic integrated circuits (PICs) technology is one of the most promising [12]. Due to the
42 compatibility with complementary metal-oxide semiconductor (CMOS) foundry processes, silicon PICs
43 can be manufactured with great efficiency at high volume [13]. Moreover, the high refractive index contrast
44 between silicon and silicon dioxide, or other surrounding media, enables the development of miniaturized
45 compact sensing devices, with the additional possibility of fabricating multiple sensors on one single chip
46 [10]. Meanwhile, silicon photonics are excellent transducers for continuous and quantitative label-free
47 biosensing [14,15], which can directly respond to affinity interactions between analyte and receptor molecules
48 in real-time. Hence, numerous silicon photonic sensing devices, such as Mach-Zehnder interferometers
49 (MZIs) [16,17], microring resonators (MRRs) [18,19], microdisk resonators [20,21], Bragg grating resonators
50 [22,23], and one-dimensional (1D) or two-dimensional (2D) photonic crystals (PhCs) [24,25] have been
51 developed over the past decades for biosensing diagnostic applications.

52 This paper reviews the literature on label-free integrated (i.e., not SPR) photonic biosensors over the last
53 20 years. An overview of the main planar integrated optical sensing configurations for label-free detection
54 is presented, emphasizing the description of these structures and corresponding sensing mechanisms.
55 Several performance-improving approaches, such as using slot, thinner or suspended waveguides, and 1.31
56 μm wavelength light sources, as well as advanced strategies by employing sub-wavelength grating (SWG)
57 waveguides and the Vernier effect method, are also introduced. A brief summary of experimental validations
58 of biomarkers and their respective detection limits (*DLs*) is listed to illustrate their dynamic ranges of sensing
59 and limitations therein. To address system operations for lab-on-a-chip diagnosis, approaches for optofluidic
60 and optoelectronic integrations on the silicon-on-insulator (SOI) substrate are mentioned including their
61 advantages and disadvantages. Finally, examples of some state-of-the-art packaged on-CMOS sensing
62 platforms are reported, showing a promising prospect for the development of fully integrated, portable,
63 lab-on-a-chip biosensing architectures for multiplexed label-free diagnostics.

64 2. Theory and Structures

65 2.1. Evanescent Field Sensing Principle

66 Leveraging the silicon-on-insulator (SOI) platform, silicon photonic biosensors rely on near-infrared
67 light confined in nanometer-scale silicon wires (known as waveguides) to sense molecular interaction events.
68 The portion of the light's electrical field traveling outside of the waveguide is referred to as the evanescent field,
69 which can interact with the surrounding volume to create an external RI sensitive region (Figure 1a). When
70 target molecules bind to receptors at the waveguide's surface, the accumulation of molecules with a different
71 refractive index changes the external RI and perturbs the evanescent field, which then further influences the
72 behavior of the guided light in the waveguide [26]. By monitoring the coupling and/or propagation properties
73 of the output light, analytes of interest can be detected in real-time (Figure 1b) [27]. Since the evanescent field
74 decays exponentially with a decay length ranging from a few tens to a few hundreds of nanometers into the
75 bulk medium, the sensing signal of an analyte captured within the decay length shows a significant difference
76 compared to the signal of an analyte floating far away from the surface [15]. Thus, based on the response
77 of the evanescent field sensor, we can distinguish the target molecules immobilized on the surface (surface
78 sensing) from those remaining in bulk solution (bulk sensing), as presented in Figure 1c.

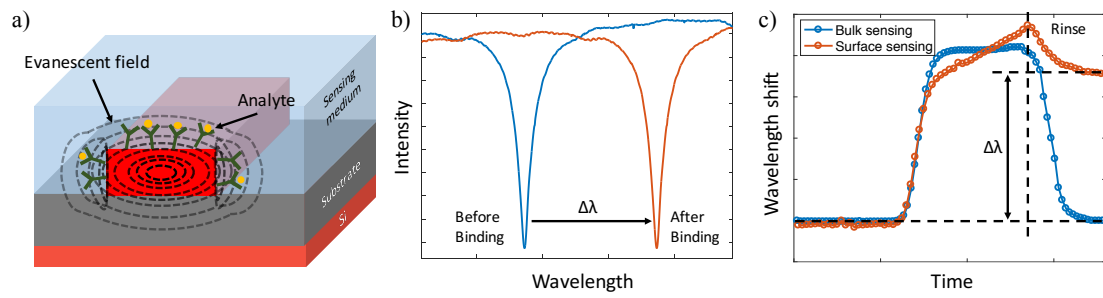


Figure 1. Principle of the evanescent field detection for a silicon photonic biosensor. (a) The evanescent field (dashed lines) around the waveguide is sensitive to the RI change caused by biological binding events at the waveguide's surface. (b) Optical transmission spectra of the sensor before (blue curve) and after (red curve) the analyte interaction, resulting in a wavelength shift ($\Delta\lambda$). (c) Sensorgrams of the sensor in bulk (blue curve) and surface (red curve), where the signals are recorded as a function of time.

Sensitivity (S) and detection limit (DL) are two important performance criteria for the evaluation of sensor performance. In evanescent field sensors, sensitivity is determined by the strength of interactions between matter and the fraction of light in solution or at the surface [15]. According to the status of target molecules, two specific types of sensitivities are defined in biosensing applications: (1) bulk sensitivity (S_{bulk}), which takes into account RI changes of the waveguide's entire cladding, and (2) surface sensitivity (S_{surf}), which assesses RI changes within the first few tens to hundreds of nanometers above the surface [26]. For the bulk sensitivity, it is defined as the slope of wavelength (or phase) shift versus the change of refractive index unit (RIU), and the shift is described by [28]:

$$\frac{\Delta\lambda}{\lambda} \text{ (or) } \frac{\Delta\phi}{\phi} = \frac{\Delta n_{\text{fluid}}}{n_g} \cdot \frac{\partial n_{\text{eff}}}{\partial n_{\text{fluid}}}, \quad (1)$$

where λ is the wavelength and ϕ is the phase of the input light, n_{fluid} is the RI of the analyte solution, and n_{eff} and n_g are the mode's effective and group indices. From Equation 1, the wavelength (or phase) shift is mainly contributed by the shift in the solution's RI (Δn_{fluid}), the dispersion (n_g) of the material and waveguide, and the mode's effective index change ($\partial n_{\text{eff}}/\partial n_{\text{fluid}}$) caused by the slight change of the mode profile [28]. The bulk sensitivity is defined as:

$$S_{\text{bulk}} = \frac{\Delta\lambda \text{ (or) } \Delta\phi}{\Delta n_{\text{fluid}}}. \quad (2)$$

As for the surface sensitivity, the definition is slightly different from the bulk one by replacing the solution's RI (n_{fluid}) with the thickness of a homogeneous adlayer on the surface (t_{adlayer}). Therefore, the expressions for the wavelength (or phase) shift and surface sensitivity are [29]:

$$\frac{\Delta\lambda}{\lambda} \text{ (or) } \frac{\Delta\phi}{\phi} = \frac{\Delta t_{\text{adlayer}}}{n_g} \cdot \frac{\partial n_{\text{eff}}}{\partial t_{\text{adlayer}}}, \quad (3)$$

$$S_{\text{surf}} = \frac{\Delta\lambda \text{ (or) } \Delta\phi}{\Delta t_{\text{adlayer}}}, \quad (4)$$

79 respectively. From Equation 3 and 4, $\partial n_{\text{eff}}/\partial t_{\text{adlayer}}$ is highly dependent on the refractive index of the adlayer
 80 material: a high RI analyte can lead to a significant effective index variation and wavelength shift even with a
 81 thin adlayer at the surface. Thus, surface sensitivity is usually defined for a specific molecule of interest and is
 82 not suitable for a general comparison among sensors operated with different biosensing assays.

The detection limit (DL) is typically specified as the minimum RI (or smallest mass) change necessary to cause a detectable change in the output signal, and defined as follows:

$$DL = \frac{3\sigma}{S} \quad (5)$$

83 where σ is the system noise floor, and S is the bulk or surface sensitivity. Since σ depends on the experimental
 84 setup and readout instrumentation, this DL is also regarded as the system's detection limit (sDL). For an
 85 evanescent field label-free biosensor, DL can be specified in three units: (1) DL in units of refractive index
 86 units (RIU) aims to characterize the sensing capability in bulk solution, which offers a rough comparison
 87 among different sensors, (2) DL in units of pg/mm^2 and (3) in units of ng/mL aim to characterize the sensing
 88 capability at sensor's surface by using surface mass density and sample concentration, respectively [15]. Due
 89 to the correlation among these DL s, the sensing capability of optical biosensors based on different bioassays
 90 can be investigated and compared.

91 2.2. Optical Biosensor Configurations

92 We select the following representative optical structures that have been reported in the literature and
 93 widely used as silicon photonic label-free biosensors.

94 2.2.1. Interferometer Based Biosensors

95 Interferometer-based biosensors constitute one of the most sensitive integrated-optic approaches by
 96 combining two very sensitive methods: waveguiding and interferometry techniques [30]. In a conventional
 97 interferometric biosensor, the guided light is split by a Y-junction into two single-mode waveguide paths,
 98 one of which containing the sample is regarded as a sensing arm and the other one is used as a reference
 99 arm. The evanescent field of the sensing arm interacts with the sample and senses the RI change at the
 100 surface, resulting in an optical phase shift. After a certain distance, the beams recombine again and cause a
 101 constructive or destructive interference at the output, where the intensity modulation corresponds to the RI
 102 difference between sample and reference arms.

103 Young and Mach-Zehnder interferometers are the most common formats for interferometric sensing
 104 techniques [27,30,31]. Since the first double-slit experiment by Thomas Young in 1801 [32], and the
 105 demonstration of the phase shift detection between two collimated beams by Ludwig Zehnder [33] and
 106 Ernst Mach [34] in 1891 and 1892, Young and Mach-Zehnder interferometric configurations have been
 107 exploited in biosensors successfully. Although both of these interferometers utilize Y-junctions to split the
 108 coherent, single mode and polarized light at the input, the output recombination of Young interferometers
 109 (YIs) is not realized like MZIs (Figure 2a) by another on-chip Y-junction. Instead, the interference light in YIs
 110 is projected on a screen or CCD camera in an off-chip way, as shown in Figure 2b.

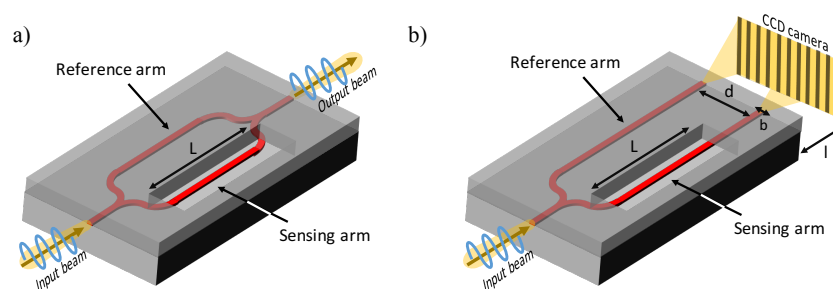


Figure 2. Interferometric biosensors. (a) Illustration of a typical Mach-Zehnder interferometer. The light is split into two arms (sensing and reference) and recombined at the output by on-chip Y-junctions. The degree of interference is proportional to the RI variation taking place on the sensing arm. (b) Illustration of a classic Young interferometer. Rather than using Y-junctions to rejoin the split beams, the light is projected from two closely spaced secondary sources onto a CCD camera, resulting in an interference pattern.

In case of a MZI sensor, the output intensity (I_{out}) is a periodically oscillating function of the phase change difference ($\Delta\phi$) of the beams from two arms with the following expression [35]:

$$I_{\text{out}} = I_{\text{sen}} + I_{\text{ref}} + 2\sqrt{I_{\text{sen}}I_{\text{ref}}}\cos(\Delta\phi + \Delta\phi_0) \quad (6)$$

where I_{sen} and I_{ref} are the intensity of the light passing through the sensing and reference arms of the MZI, respectively, and $\Delta\phi_0$ is the initial phase difference due to the unbalance of the two arms. The phase difference caused by the external RI change at the wavelength λ is calculated as:

$$\Delta\phi = \frac{2\pi}{\lambda} L (n_{\text{eff}}^{\text{sen}} - n_{\text{eff}}^{\text{ref}}) \quad (7)$$

where L is the effective detection length of the sensing arm, and $n_{\text{eff}}^{\text{sen}}$ and $n_{\text{eff}}^{\text{ref}}$ are the effective propagation indices of the guided modes in the sensing and reference arms, respectively. As for the YI sensor, since not a single intensity, but an interference pattern (so-called interferogram) is detected at the output, the optical path length difference from two secondary sources is varying along the propagation direction (y -axis) [30]. Thus, Equation 6 should be rewritten for YI sensors as [36]:

$$I_{\text{out}}(y) = \frac{\sin^2(b\pi y/\lambda l)}{(b\pi y/\lambda l)^2} \left[I_{\text{sen}} + I_{\text{ref}} + 2\sqrt{I_{\text{sen}}I_{\text{ref}}} \cos\left(\frac{\lambda l}{2\pi d} y + \Delta\phi + \Delta\phi_0\right) \right] \quad (8)$$

where b , d and l are the width of a single slit, the distance of two secondary sources and the distance from sources to the detector surface, respectively (as shown in Figure 2b). In this case, the phase difference is expressed as:

$$\Delta\phi = \frac{2\pi}{\lambda} \left[xd/l - L (n_{\text{eff}}^{\text{sen}} - n_{\text{eff}}^{\text{ref}}) \right] \quad (9)$$

111 where x denotes the position of the interferogram on the camera. The fringe pattern moves laterally at the
 112 output. The sensitivity of interferometric sensors is defined as the change in phase caused by the change in
 113 the RIU of the cladding above the sensing arm. According to Equation 7 and Equation 9, a longer interaction
 114 length (L) in the sensing arm can increase the sensitivity [37]. However, due to the cosine-dependent intensity
 115 function of the interferometric curve, the intensity response is non-linear: a higher signal change at the
 116 quadrature point is observed than the one near the curve extreme of the cosine function. Moreover, false
 117 positive signals occur when input source fluctuations or temperature variations happen, which strongly
 118 influence the reliability of the interferometric sensor, especially with long sensing arms [38]. Thus, additional
 119 modulation approaches are usually needed to tune the phase difference between the arms for interferometer
 120 sensors.

121 The first biosensing application using integrated MZIs was reported by Heideman et al. in the early 1990s
 122 [39,40]. Since then, remarkable progress has been achieved in the development of MZI sensors. Different
 123 configurations with a variety of fabrication materials from Si_3N_4 [40,41], SiO_2 [42], Si [43,44] to polymers
 124 [45,46], and even liquid [47] were employed successfully, showing a DL down to $10^{-6} \sim 10^{-7}$ RIU. In parallel,
 125 chip-integrated YIs have also shown the ability of biomolecule measurement, yielding a comparable DL to
 126 the MZI sensor [48,49]. In 2000, a follow-up work by Brandenburg et al. reduced the DL of YI sensors to $9 \times$
 127 10^{-8} RIU by employing silicon oxynitride as waveguides [50]. Seven years later, Ta_2O_5 -based YIs have been
 128 reported by Schmitt et al. to further improve the sensing ability, with the lowest published DL of 9×10^{-9}
 129 RIU [51]. Moreover, polymeric materials were also applied to YI sensors in the last few years, which offer a
 130 low-cost, mass-produced manufacturing method with a satisfactory sensitivity [52,53].

131 More recently, Lechuga et al. have introduced a BiModal waveguide (BiMW) interferometer for
 132 biosensing applications [38,54,55]. Instead of splitting the beam into different arms, the light excites two
 133 different modes by a step-junction, and molecular interactions are monitored by the bimodal section. Due to
 134 the difference of modal overlap with the analyte, phase changes in two modes introduced by the RI change are
 135 distinct, leading to the interference between the two guided modes. The reported DL of the BiMW sensor is as
 136 low as 2.5×10^{-7} RIU [54] comparable to other interferometric sensors. However, these devices usually need
 137 a large footprint, around 5 to 10 mm in length, which limits the density of on-chip sensors for multiplexable
 138 detections.

139 2.2.2. Resonant Microcavity Based Biosensors

Optical microcavity resonators have been investigated as an emerging sensing technology due to their potential for highly-compact sensing arrays. In a microcavity resonator structure, incident light propagating in an input waveguide or tapered fiber is coupled into the microcavity via the evanescent field. Then, coupled light passes through the cavity in the form of whispering gallery modes (WGMs) or circulating waveguide modes with multiple round-trips, resulting in optical interference at specific wavelengths of light, as shown in Figure 3a by the resonant condition:

$$\lambda = \frac{2\pi r n_{\text{eff}}}{m} \quad (10)$$

140 where λ is the resonant wavelength, r is the radius of the resonator, n_{eff} is the resonator effective refractive
 141 index, and m is an integer. The positions of resonant peaks are related to the RI near the resonator surface
 142 and shift due to the change of n_{eff} , which can be monitored by scanning the wavelength or by measuring the
 143 intensity at a single wavelength.

Unlike interferometric biosensors, the interaction of light and analyte is no longer determined by the length of the sensing waveguide, but rather by the characteristic time of the energy stored inside the resonator, which is characterized by the quality factor (Q -factor) [15]. Q -factor describes the photon lifetime in the resonator and represents the number of oscillations before the energy has decayed to 37% ($1/e$). Therefore, Q -factor incorporates the distributed loss of a resonator and is approximated by dividing the resonant wavelength by its full width at half maximum (FWHM) [28]:

$$Q = \omega \frac{\varepsilon}{\partial \varepsilon / \partial t} = \frac{2\pi n_g \cdot 4.34}{\lambda \cdot \alpha_{\text{(dB/m)}}} \approx \frac{\lambda}{\Delta \lambda_{\text{FWHM}}} \quad (11)$$

where ω is the resonant frequency, ε is the energy of the resonant mode, n_g is the group index, α is the total distributed loss in the resonator, and $\Delta \lambda_{\text{FWHM}}$ is the FWHM bandwidth of the resonance peak. A higher Q -factor indicates that light stays in the resonator longer and interacts more with the analyte. Moreover, White et al. have proved that having a high Q -factor is advantageous in reducing the noise of the sensor (σ), which further improves the DL [56]. As mentioned before, the DL (or sDL) relies much on the measurement system including curve fitting methods and limitations from light sources or detectors, which makes it difficult to have an objective comparison between sensors with different assays and experimental systems [57]. As a consequence, intrinsic detection limit (iDL) was introduced as a substitute for resonant sensors, which is only dependent on intrinsic characteristics, i.e., the resonance linewidth, and defined by [58]:

$$iDL = \frac{\lambda}{Q \cdot S} \quad (12)$$

144 where λ , Q , and S are the sensor's resonant wavelength, quality factor, and sensitivity, respectively. By
 145 replacing S with S_{bulk} or S_{surf} , the bulk or surface iDL can be represented.

146 Several types of planar resonant microcavity-based configurations have been implemented so far for
 147 biosensing since the introduction from two theoretical papers in 2001 [59,60], such as microring (MRR) [61],
 148 microdisk [62] and microtoroid [63] shaped resonators (Figure 3). Similar to interferometers, microcavity
 149 resonators can be made of Si_3N_4 [64,65], SiO_2 [66,67], Si [18,68], and polymer [69,70] as well. Although
 150 resonator-based biosensors enable dense on-chip integration and offer a similar DL of $10^{-5} \sim 10^{-7}$ RIU
 151 [18,71], their Q -factors (except toroid resonators) are relatively low especially with water cladding (around
 152 10^4) due to the high optical loss, such as side-wall scattering, bend radiation, mode mismatch and material
 153 absorption [72]. Microsphere-based ring resonators [73,74] and capillary-based opto-fluidic ring resonators
 154 (OFRR) [75] have been recently introduced, supporting improved Q -factors over 10^6 with DL s on the order of
 155 10^{-7} RIU, and applied in a wide sensing range from pesticide [76], cancer [77], to bacteria [78]. However, due
 156 to three-dimensional architectures, these devices are not suitable for on-chip fabrication and microfluidics
 157 integration. Besides, optical interrogation of these resonators requires meticulous positioning of optical fibers
 158 with nanometer precision and alignment [27].

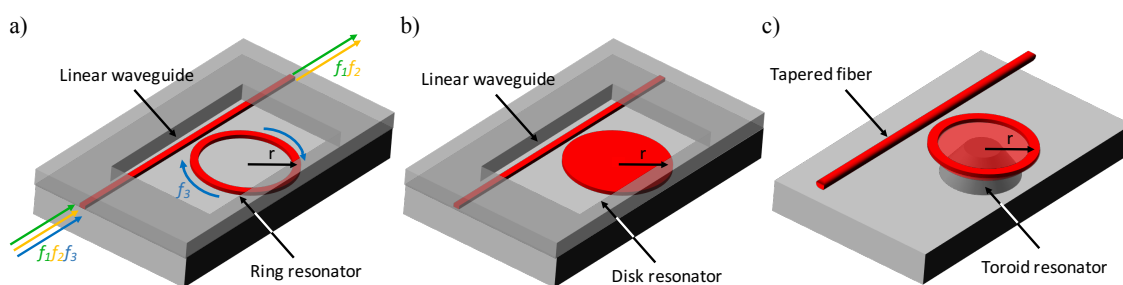


Figure 3. Planar resonant microcavity biosensors. (a) Illustration of a conventional MRR sensor. By using a bus waveguide, guided light is coupled into the resonator at a frequency corresponding to the resonant condition. (b) Illustration of a microdisk resonator sensor. (c) Illustration of a microtoroid resonator sensor. This structure is coupled by a low-loss tapered fiber, exhibiting an ultrahigh Q -factor over 10^8 [79].

159 2.2.3. Photonic Crystal Based Biosensors

160 A photonic crystal (PhC) waveguide consists of periodically repeating arrays of dielectric structures,
 161 forming periodic variations in the refractive index. The periodicity is on the order of the optical wavelength
 162 and stops a range of wavelengths propagating through the PhC, resulting in a photonic bandgap on the
 163 transmission (or reflection) spectrum. By introducing a defect into the PhC structure, a defect mode at a
 164 particular wavelength is formed and resonantly confined in the defect region, which leads to a sharp peak
 165 within the bandgap. Due to the strong optical confinement, light is concentrated in a minimal volume near the
 166 defect, enabling an intense light-matter interaction area. A tiny volume of analytes immobilized surrounding
 167 the defect can induce a noticeable shift of the resonance wavelength and provide a measurable response.
 168 Hence, in the past few years, PhC based biosensors are regarded as a promising and novel technology that has
 169 gained much attention [80–82].

170 The periodicity of a PhC structure can vary from one-dimensional (1D), two-dimensional (2D) to
 171 three-dimensional (3D). One-dimensional PhCs are the most straightforward architecture analyzed by Lord
 172 Rayleigh as early as 1887. These structures consist of different material layers with high and low refractive
 173 indices alternatively (Figure 4a) and are usually fabricated by layer-by-layer deposition, spin coating, or
 174 photolithography methods [83]. In 1987, Yablonovitch [84] and John [85] reported the detailed research on
 175 PhCs separately, proposing the concept of photonic bandgaps in 2D and 3D structures. 2D and 3D PhCs
 176 exhibit their periodicity in two and three spatial directions as shown in Figure 4b and 4c, which need complex
 177 manufacturing techniques like photolithography, etching, and particle self-assembly, etc [83]. Although the
 178 complexity of the manufacturing process of 1D PhC devices is low, a well-collimated beam is usually required
 179 for sensing approaches, especially for high Q -factor devices, which needs the sensing area to be relatively
 180 large, compared to 2D or 3D ones [86].

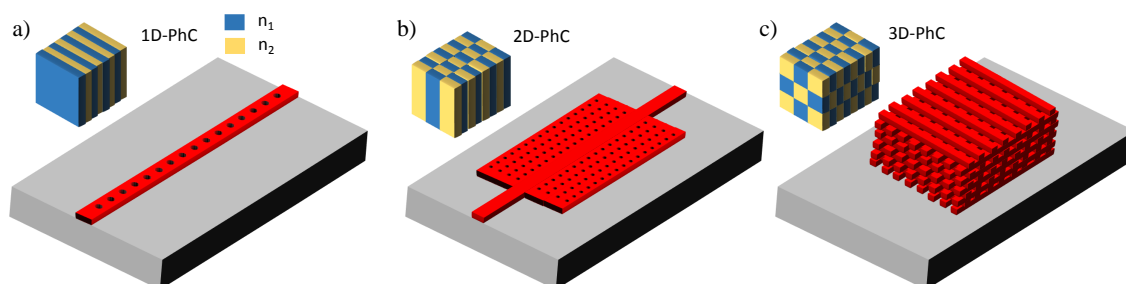


Figure 4. Illustration of photonic crystals in (a) 1D, (b) 2D, (c) 3D conformations. Insert: Schematic representation of each format showing the periodic arrangements, different colors represent materials with different indices.

181 PhC biosensors were first developed using TiO₂-coated polymer gratings by Cunningham et al.
182 in the early 2000s, offering an inexpensive manufacturing technique on plastic films [87–89]. At the
183 same time, Si-based PhC devices in the SOI platform were also investigated and have developed rapidly
184 leveraging electron beam lithography (e-beam) technology, including 1D PhC [90–92], 2D PhC [25,80] based
185 architectures, for biomolecule detections. Chow et al. demonstrated an ultra-compact PhC sensor with a
186 sensing area of 10 μm², enabling a *DL* of better than 2×10^{-3} RIU and a *Q*-factor of 400 in 2004 [80]. Later in
187 2010, Skivesen et al. achieved an improved *DL* of 6.75×10^{-4} RIU by tracking sharp fringes appearing in the
188 slow-light regime near the edge of the guided band [93]. In the same year, Kang et al. increased the sensing
189 surface area to the defect region of PhCs by introducing multiplehole defects (MHDs), showing an enhanced
190 sensitivity compared to PhCs with single hole defects (SHDs) [94,95]. Qin et al. incorporated the concept of
191 MHDs to the slow-light MZI-based biosensor, showing a thirteen-fold higher bulk sensitivity than traditional
192 MZI biosensors of 115000 rad/RIU-cm [96]. Lo et al. announced an optical biosensor based on a 1D-PhC
193 microring resonator (PhCR) with enhanced detection sensitivity in 2017 [97]. By introducing the 1D PhC
194 geometry in a MRR's waveguide, the light-matter interaction is strongly improved since the PhCR can detect
195 the presence of analyte both inside 1D holes and on the top surface [97].

196 Compared to interferometric or other resonant biosensors, PhC sensors tend to have lower sensitivities
197 ranging from 10^{-2} to 10^{-4} RIU. However, PhC sensors can be readily integrated onto a chip with high density,
198 and are suitable for detection with extremely limited sample volumes (on the order of femtoliter). Recently,
199 a new trend of PhC sensor development is to achieve multi-analyte detection capability on a single chip.
200 Several 1D and 2D PhC-based sensor arrays were developed [98–101]. In 2017, Zhang et al. designed a highly
201 sensitive on-chip multichannel sensor array by integrating eight 1D PhC cavities connected by additional
202 bandgap filters, showing improvements in size, integration density, sensitivity, and ease of fabrication [102].

203 2.2.4. Bragg Grating Based Biosensors

The Bragg grating, a fundamental component for the purpose of wavelength selection, has been investigated for use in optical communications, such as filters, semiconductor lasers and fibers for a long time [72], and recently into biosensing applications [22,103]. Similar to 1D photonic crystals, a Bragg grating is a structure with a periodic modulation of the effective RI in the propagation direction of the optical mode, as shown in Figure 5. By alternating the material with different indices or physical dimensions (known as the corrugation) of the waveguide, the desired index modulation is achieved. A reflection of the guided light occurs at each index-changed boundary as presented in Figure 5a, and the repeated modulations of the effective index multiply the distributed reflection, resulting in a stop band at one specific wavelength in the transmission spectrum, where light is strongly reflected. The center wavelength of the stop band, namely the Bragg wavelength, is given as:

$$\lambda = 2\Lambda n_{\text{eff}} \quad (13)$$

204 where Λ is the period, and n_{eff} is the average effective index of Bragg gratings. If a phase-shifted cavity is
205 introduced in the middle of the gratings, as illustrated in Figure 5b, a narrow resonant transmission peak will
206 appear within the stop band [104], which can be utilized for RI change monitoring.

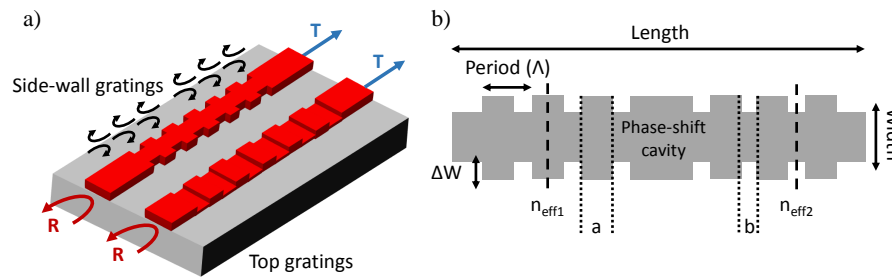


Figure 5. Bragg grating biosensors. (a) Illustration of two types of Bragg grating devices with side-wall or top gratings. R and T are the grating's reflection and transmission. The 180° arrows represent the numerous reflections throughout the grating. (b) Schematic of a phase-shifted Bragg grating device. Λ is the period, ΔW is the width of the corrugation, a or b and $n_{\text{eff}1}$ or $n_{\text{eff}2}$ are the length and the effective index of the high or low index section.

207 Fiber Bragg gratings (FBGs) have attracted a great deal of attention in recent years for biosensing
 208 applications, due to the low price and ease of signal transmission of fiber materials. In order to improve
 209 the sensing performance, numerous studies have been attempted to expose the evanescent field from
 210 the fiber core, such as side-polishing or surface-etching strategies, achieving a DL down to $10^{-5} \sim 10^{-6}$
 211 RIU [105–107]. Recent advances in Bragg gratings have led to the on-chip integration realized in the SOI
 212 platform, firstly demonstrated by Murphy et al. in 2001 [108]. A theoretical demonstration of biosensing
 213 capability of SOI-based Bragg gratings was announced by Passaro et al. in 2008 [109]. By periodically
 214 etching the top surface of the silicon waveguide, a submicrometer integrated optical Bragg grating sensor is
 215 proposed with a simulated DL of approximately 10^{-4} RIU [109]. One year later, Jugessur et al. developed a
 216 uniform Bragg grating biosensor integrated with microfluidics for RI index sensing by using vertical grating
 217 side-edges proving potential for lab-on-a-chip applications [22]. Prabhathan et al. proposed the concept of a
 218 phase-shifted vertical side wall gratings for biosensing in the same year with a theoretical DL of 8.1×10^{-5}
 219 RIU [23]. In 2013, Fard et al. fabricated and characterized the strip-waveguide based phase-shifted Bragg
 220 grating in the SOI platform, and the Q -factor was measured to be 27600, which led to a experimental iDL of
 221 9.3×10^{-4} RIU [110].

222 2.2.5. Section summary

Figure 6 summarizes the simulated transmission spectra of previously described optical configurations in the field of silicon photonic biosensors. As a concept illustration, we only consider the intrinsic losses in each device. As shown in Figure 6, MZI (blue curve) and MRR (red curve) sensors present periodic spectra. The spacing between optical wavelengths of two consecutive transmitted optical intensity minima is defined as the free spectral range (FSR) and given by:

$$\Delta\lambda_{\text{FSR}} = \frac{\lambda^2}{n_g \cdot L} \quad (14)$$

223 where λ is the wavelength of the light source, n_g is the waveguide group index, and L is the length difference
 224 of two arms in the MZI or the perimeter of the MRR. As for the transmission spectrum of the PhC or Bragg
 225 grating (yellow curve), due to the existence of the defect or phase-shifted cavity, a sharp FSR-free resonant
 226 peak appears in the middle of the stop band with a narrow FWHM corresponding to the high Q -factor. By
 227 interrogating the wavelength (phase) shift or intensity change of these peaks in the transmission plots, the RI
 228 change caused by the analyte within the evanescent field can be monitored in real-time. Generally, compared
 229 to other geometries, a MZI-based optical sensor is one of the simplest configurable devices with similar sensor
 230 performance. However, disadvantages such as large footprint, high-temperature sensitivity, and the need for
 231 additional modulation methods hinder the development of on-chip MZI sensing arrays. Resonator-based
 232 sensors, like MRRs, microdisks, PhCs and Bragg gratings, are more suitable for the integrated sensing platform

233 with a high density due to their small sizes. Different from MRRs, PhCs and Bragg gratings have a high Q -factor
 234 due to the elimination of bending (mode and radiation) losses, thus an improved iDL , even though their
 235 sensitivities are comparable. Although silicon-based architectures have been successfully applied for the
 236 detection of cell secretions [111], virus [112], protein biomarkers [11], and nucleic acids successfully [113,114],
 237 a lower detection limit with a higher sensitivity is still required for current clinical diagnostic tests [115].

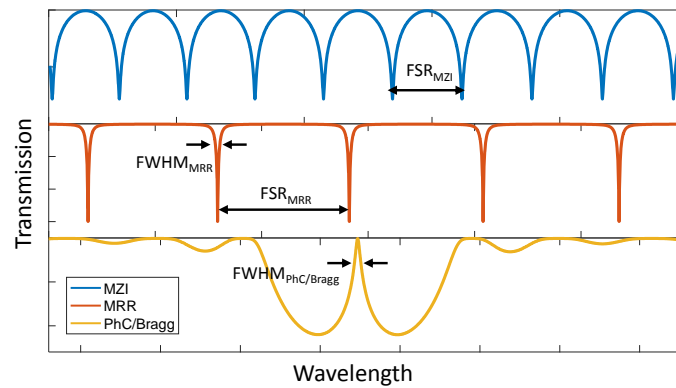


Figure 6. Simulated transmission spectra of different optical configurations, including MZI (blue curve), MRR (red curve), defected PhC or phase-shifted Bragg grating (yellow curve) sensors. The optical insertion loss caused by input and output coupling devices has been eliminated. The full width at half maximum (FWHM) indicates the optical wavelength width of the resonant peak at which the transmitted intensity is equal to half (-3 dB) of its maximum value.

238 3. Performance-Improved Strategies

239 In this section, we outline early and emerging strategies in the development of SOI-based biosensor
 240 performance, including the use of new geometries of optical waveguides, and different polarizations or
 241 wavelengths of light sources. Furthermore, an overall performance metrics comparison is presented at the
 242 end, which includes proposed sensing architectures with or without their performance improved strategies.

243 3.1. Fundamental Approaches

244 3.1.1. Transverse Magnetic Mode

245 Due to the large evanescent field component traveling above the waveguide, optical sensors in the
 246 quasi-transverse magnetic (TM) mode present an improved sensitivity to that of the quasi-transverse electric
 247 (TE) mode at $1.55 \mu\text{m}$ in conventional 220 nm -thick SOI waveguides [43,116]. Figure 7 below shows the
 248 electric field intensity distributions of the TE and TM modes propagating in a $220 \times 500 \text{ nm}$ waveguide. Most
 249 of the field intensity is above and beneath the waveguide core (in the cladding and substrate) in the TM
 250 mode, offering a higher light-matter interaction strength. Moreover, the TM mode also experiences less
 251 scattering loss, which is usually caused by sidewall roughness, compared to the TE mode [29]. Because of
 252 these unique properties of TM mode based waveguides, a large number of evanescent field biosensors have
 253 been attempted in the TM mode for higher susceptibility to RI changes.

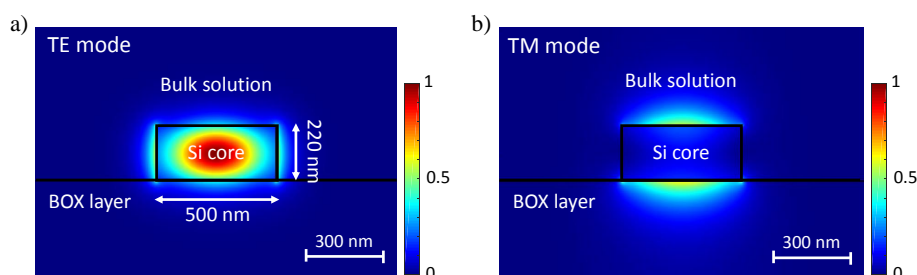


Figure 7. Illustration of electric field intensity distributions of the (a) TE and (b) TM modes in a 200×500 nm silicon waveguide at 1550 nm wavelengths. The Si waveguide core ($n_{\text{eff}} = 3.47$) is exposed to the surrounding medium with a refractive index of 1.33 above a $2 \mu\text{m}$ thick buried oxide layer (BOX) with a refractive index of 1.44.

254 For the MZI configuration, Densmore et al. have made many contributions in surface biosensing by
 255 introducing TM polarized light [17,44,117]. These TM mode based MZI biosensors achieved a minimum
 256 detectable mass of ~ 10 fg of streptavidin [17] and ~ 0.5 fg of anti-rabbit IgG [44], respectively. In 2008,
 257 Zinoviev et al. developed a MZI-based biosensor by using Si_3N_4 , where the lowest DL in the variation of the
 258 RI for the TM polarization is found to be 10^{-7} RIU [12]. Similarly, TM mode based resonant microcavities
 259 have been investigated as alternatives to their TE mode counterparts. An investigation of silicon MRR based
 260 biosensor arrays is reported by Xu et al. in 2010 with an experimental sensitivity of 135 nm/RIU; binding
 261 interactions between complementary IgG protein pairs was monitored with a concentration down to 20 pM
 262 by utilizing TM-polarized light [118]. Fard et al. reported a sensitivity enhanced TM mode MRR biosensor by
 263 decreasing the thickness of silicon waveguides to 150 nm, resulting in sensitivities as high as 270 nm/RIU and
 264 437.5 pm/nm for bulk and surface analytes [19]. In 2013, Grist et al. introduced Si-based microdisk resonators
 265 for label-free biosensing, and experimental results showed sensitivities of 26 nm/RIU and 142 nm/RIU, and
 266 Q-factors of 3.3×10^4 and 1.6×10^4 for the TE and TM modes, respectively [21].

267 3.1.2. Slot Waveguides

268 A slot-waveguide device consists of two high index rails separated by a low index slot [64]. Because of
 269 the high concentration of the electric field intensity within the slot, slot-waveguide based structures stand
 270 out for the potential to enhance sensitivity for optical biosensors. As presented in Figure 8a, light is strongly
 271 confined in the slot region. Thus, compared to conventional waveguides, a stronger light-matter interaction
 272 can be obtained in this region, leading to an improved sensitivity. Also, slot-waveguide based structures are
 273 also CMOS compatible which enables miniaturization and integration for a lab-on-a-chip platform with low
 274 cost [37,119].

275 In 2005, Baehr-Jones et al. designed, fabricated and characterized MRRs based on slot-waveguide
 276 geometries in SOI materials [120]. Two years later, Barrios et al. pioneered the development of slot-waveguide
 277 biosensors by using Si_3N_4 -based MRRs with a slot width of 200 nm for both the waveguide and resonator
 278 [121]. A highly improved bulk sensitivity of 212 nm/RIU with a Q-factor of 1800 and DL of 2×10^{-4} RIU
 279 is achieved [121]. In 2010, an integrated optical Si_3N_4 slot-waveguide MRR sensor array was reported by
 280 Carlborg et al. for multiplexed label-free biosensing, yielding a bulk DL of 5×10^{-6} RIU and a surface mass
 281 density DL of $0.9 \text{ pg}/\text{mm}^2$ [64]. In the same year, Claes et al. presented a double-bus MRR comprised of
 282 SOI-based slot-waveguides with 104 nm slot width (Figure 8b), a sensitivity of 298 nm/RIU and DL of $4.2 \times$
 283 10^{-5} RIU are obtained for changes in the RI of the top cladding [122]. In 2016, Taniguchi et al. developed
 284 MRR biosensors with silicon nitride slot waveguides due to the lower temperature coefficient, achieving
 285 a detection of prostate specific antigen (PSA) with the DL of 1×10^{-8} g/mL, which is the concentration
 286 strongly suspicious for prostate cancer [123]. In the same year, Zhang et al. investigated a racetrack all-pass
 287 slot-waveguide MRR showing a V-shaped resonant spectrum modulated by the classical frequency comb,
 288 by tracking the spectrum envelope wavelength shift, and an ultra-high sensitivity up to 1300 nm/RIU is

received [124]. However, the sensing strategy is based on the wavelength-sensing critical coupling condition, which makes the sensitivity very wavelength dependent. A horizontal slot waveguide configuration was proposed by Barrios for Si-based microdisk resonator biosensors for the TM polarization in 2006, showing an expected Q -factor of 15000 with a minimum DL of 3×10^{-8} RIU [125]. Four years later, Lee et al. followed up that concept and demonstrated a horizontal air-slot microdisk resonator for label-free biosensing based on silicon nitride as shown in Figure 8d; a Q -factor of 7000 is obtained in the TM mode with a DL of 30 ng/mL for biotin-streptavidin interactions [126]. Kim et al. reported a luminescent horizontal air-slot microdisk resonator sensor based on silicon-rich nitride (SRN) in the 800-nm wavelength range; a surface sensitivity of 4.79 nm/($\mu\text{m}\cdot\text{mL}$) is achieved by introducing biotin-streptavidin model [127].

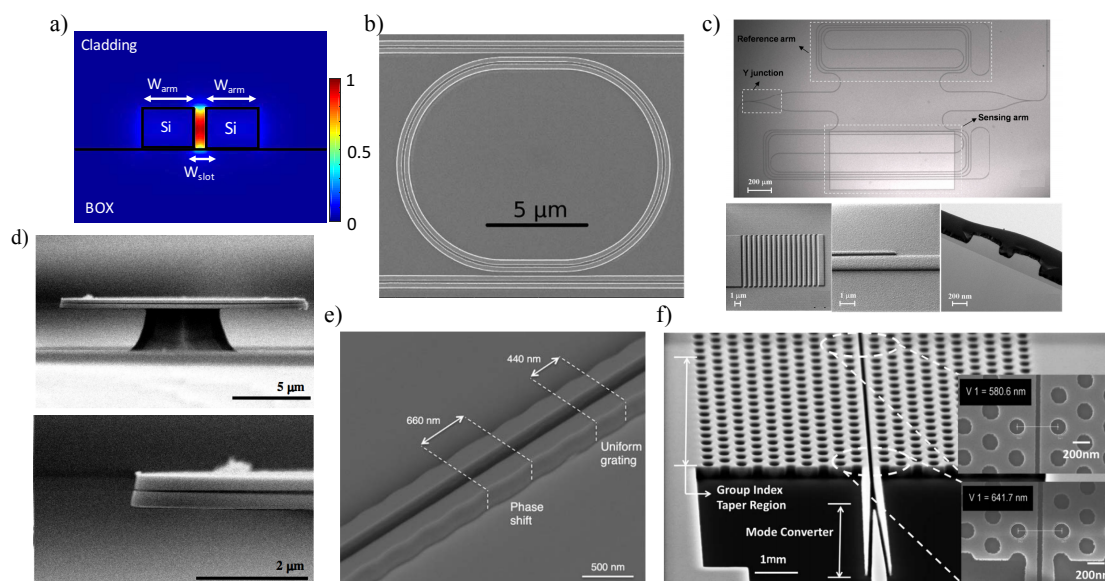


Figure 8. (a) Cross-section of the electric field intensity distribution of a slot-waveguide immersed in water. (b) Top-view scanning electron microscope (SEM) image of the slot-waveguide-based MRR. Figure adapted with permission from Ref. [122]. (c) Microscopic and SEM images of the MZI biosensor with a slot-waveguide sensing arm. Figure adapted with permission from Ref. [128]. (d) SEM images of the fabricated slot disk after the whole sensing process. Figure adapted with permission from Ref. [126]. (e) SEM image showing a phase-shifted Bragg grating sensor, the spacing with the phase shift is 600 nm, corresponding to 1.5 times the grating period. Figure adapted with permission from Ref. [129]. (f) SEM images of fabricated PC slot-waveguide device, showing a slot entirely across the device. Figure adapted with permission from Ref. [130].

Slotted PhCs combine the advantages of light confinement in the slot waveguide with the temporal confinement of light by a PhC in a single structure, offering more light interactions with the analyte [131]. Di Falco et al. reported a sensitivity improved (over 1500 nm/RIU) label-free biosensor by applying a PhC to slot geometry with a high Q -factor of 50000 and DL of 7.8×10^{-6} RIU in 2009 [132]. Jágerská et al. and Lai et al. (Figure 8f) expanded the application of slotted PhCs for gas detections, obtaining a DL of 10^{-5} RIU for a variety of gases [133] and a methane concentration of 100 ppm [130], respectively.

Plenty of work has been reported by using MZI devices with slotted sensing arms for the pursuit of a high sensitivity. In 2012, Tu et al. presented an athermal MZI biosensor based on Si_3N_4 slot waveguides (see Figure 8c); the measured bulk sensitivity and DL reach $1730(2\pi)/\text{RIU}$ and 1.29×10^{-5} RIU, respectively [128]. One year later, they followed up the investigation for biosensing by using a biotin-streptavidin binding model system, and demonstrated a DL down to 1 pg/mL of streptavidin solutions [134]. Furthermore, they also investigated the biosensor for specific detection by employing the methylation of death-associated protein kinase (DAPK) gene, showing a discriminated concentration as low as 1 nM [134]. In 2015, Sun et al. developed a MZI sensor employing an ultra-compact double-slot hybrid plasmonic (DSHP) waveguide as an

312 active sensing arm [135]. By introducing a DSHP waveguide with two open nano-slots between a high-index
313 Si ridge and two silver strips, a high optical confinement with low propagation loss was achieved, showing a
314 sensitivity as high as 1061 nm/RIU [135].

315 Recently, Wang et al. presented a slot-waveguide based biosensor using phase-shifted Bragg gratings
316 [129]. As presented in Figure 8e, the Bragg gratings with sidewall corrugations created a sharp resonant peak
317 within the stop band by introducing a phase shift. A salt solutions assay demonstrated a sensitivity of 340
318 nm/RIU and Q -factor of 1.5×10^4 , enabling a low iDL of 3×10^{-4} RIU [129].

319 3.1.3. Thinner Waveguides

320 Using thinner waveguides can lead to a lower optical confinement of the guided mode, resulting in a
321 deeper penetration of the evanescent field into the surrounding medium, as seen in Figure 9a. Thus, more
322 field overlap with biomolecules at the waveguide's surface is achieved. In 2006, Densmore et al. theoretically
323 demonstrated that thinner SOI waveguides have higher sensitivities over devices both to bulk homogeneous
324 solutions and thin adsorbed biomolecule layers [43]. Afterward, Fard et al. investigated an ultra-thin TE
325 MRR sensor using the smallest available thickness (90 nm) offered by multi-project wafer (MPW) foundries,
326 obtaining a sensitivity over 100 nm/RIU with the iDL on the order of 5×10^{-4} RIU [136]. Moreover, due
327 to the index of the water cladding decreasing with rising temperature which is opposite to the Si core and
328 SiO₂ substrate materials, ultra-thin TE MRR sensors show increased stability in the presence of temperature
329 variations as compared to the traditional 220 nm thick sensors [136].

330 3.1.4. Suspended Waveguides

331 Another method to enhance the overlap between the evanescent field and analyte is introducing
332 suspended waveguides, by replacing the BOX substrate with lower-index materials (e.g., air and water).
333 In 2000, Veldhuis et al. theoretically proposed that the sensing performance can be improved by using a
334 suspended silicon waveguide technology, where the sensitivity is enhanced by a factor of 1.35 [137]. After that,
335 many suspended sensors were reported successively leveraging the SOI platform. Wang et al. demonstrated
336 an ultra-small suspended microdisk with a radius of 0.8 μm sitting on a SiO₂ pedestal for optical sensing,
337 presenting a measured sensitivity of 130 nm/RIU in 2013 [138]. Soon later, a suspended TM-MRR biosensor to
338 increase the surface binding area and light-matter interaction was reported by Hu et al. (Figure 9b), showing a
339 near 3-fold increased response to bulk RI changes (290 nm/RIU) and 2-fold increased response to the capture
340 of targets at the surface as compared to conventional MRRs on SiO₂ (102 nm/RIU) [139]. Taha et al. recently
341 developed a centimeter-scale MZI sensor based on SOI platform by introducing a fully suspended waveguide
342 as the sensing arm, obtaining a bulk sensitivity of 740 nm/RIU with a corresponding iDL of $\sim 4 \times 10^{-5}$ RIU
343 [140].

344 3.1.5. 1310 nm Light Sources

345 For label-free biosensing, one way to improve the limits of detection of silicon photonic sensors for
346 medical diagnostic applications is enhancing the intrinsic sensor performance [29]. According to Equation 12,
347 iDL shows a reciprocal relation to its Q -factor and S . Thus, having a large Q -factor or sensitivity value can
348 effectively improve the iDL . The Q -factor can be interpreted as the total distributed loss of the device based
349 on Equation 11, and the loss originates from waveguide scattering, material absorption (waveguide and
350 analyte), waveguide radiation, mode mismatch, etc [28]. Among them, water absorption is the predominant
351 loss for silicon photonic biosensors at 1550 nm wavelengths since many analytes of interest are found in
352 aqueous solutions. Kou et al. observed that water absorption is approximately 10 times lower around 1310
353 nm wavelengths compared to 1550 nm ones [141]. By assuming an ideal Fabry-Perot cavity with the light
354 traveling entirely in the water, where no other loss mechanism exists, a fundamental limit for water-based
355 sensors was calculated by Chrostowski et al., showing an intrinsic limit of detection of 2.4×10^{-4} RIU at 1550
356 nm and 2.4×10^{-5} RIU at 1310 nm, respectively in Figure 9c [28].

357 Various silicon photonic biosensors for 1310 nm wavelengths have been reported by Schmidt et al. in
358 2014, including MRRs in the TE and TM modes, and Bragg gratings in the TM mode [29]. Experimental

359 characterizations result in a measured Q -factor of 8389, bulk sensitivity of 90 nm/RIU, and iDL of $1.49 \times$
 360 10^{-3} RIU for the TE mode MRR, and a Q -factor of 33463, bulk sensitivity of 113 nm/RIU, and iDL of $3.47 \times$
 361 10^{-4} RIU for the TM mode MRR. For TM mode Bragg gratings, a high Q -factor of 76320 with a bulk sensitivity
 362 of 106 nm/RIU and iDL of 1.62×10^{-4} RIU is achieved. In 2016, Melnik et al. investigated a MZI biosensor
 363 based on polyimide waveguides at the central wavelength of 1310 nm for human immunoglobulin G (hIgG)
 364 detection, allowing detecting concentrations down to 3.1 nM and 100 pM by label-free and labeled methods,
 365 respectively [142].

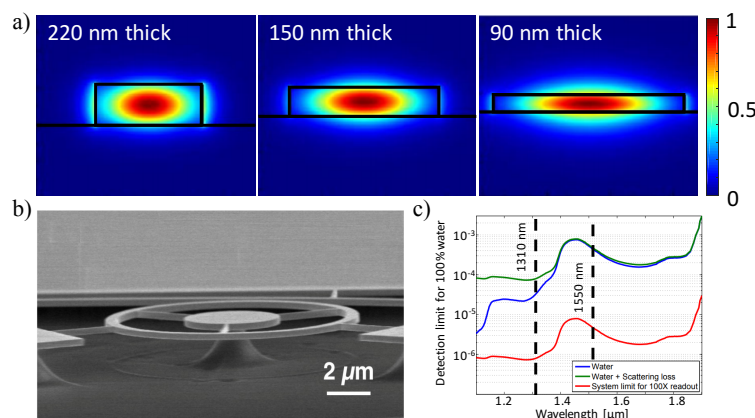


Figure 9. (a) Electric field intensity distributions of a TE mode for 90, 150 and 220 nm thick silicon cores. Figure adapted with permission from Ref. [29]. (b) Tilted SEM image of an MRR after suspension. The MRR is supported by trusses with a width of 100 nm and a height of 260 nm. Figure adapted with permission from Ref. [139]. (c) Fundamental DL plots for water-based sensors at 1310 and 1550 nm wavelengths. Highest predicted DL for water absorption limited sensing is presented (blue line). Waveguide scattering is added and assumed to contribute 5 dB/cm loss at 1550 nm, and scale as $1/\lambda^4$ at other wavelengths (green line). Finally, the sDL is shown (red line) with a wavelength readout precision 100-fold better than the resonator linewidth. Figure adapted with permission from Ref. [28].

366 3.2. Advanced Approaches

367 3.2.1. Sub Wavelength Grating Waveguides

368 A novel and appealing strategy, which allows customizing optical properties by varying the waveguide
 369 geometry, is using sub-wavelength gratings (SWG) [143]. Since the first demonstrations of an optical
 370 waveguide with an SWG metamaterial core by the National Research Council of Canada (NRC) in 2006
 371 [144–146], SWG waveguides have attracted intense research interest due to their unique potentials to control
 372 light propagation in planar waveguides, and been considered to be critical components for developing
 373 the next generation of optical communication, biomedical, quantum and sensing technologies [147,148].
 374 Although similar to Bragg gratings, SWG waveguides also consist of the periodic structure of their core,
 375 the period (Λ) is much smaller than the Bragg condition, i.e., $\Lambda \ll \lambda/(2n_{\text{eff}})$. Thus, a true lossless mode is
 376 supported in SWG waveguides because the reflection and diffraction effects are suppressed [149]. The SWG
 377 waveguide core is commonly fabricated by interleaving the high index block (n_1) with low index materials
 378 (n_2), such as SiO_2 , SU-8, air or water, as one period (a few hundred nanometers in length), as shown in
 379 Figure 10a. By having a reduced mode effective index step, the guided light propagates in SWG waveguides
 380 similar to the one in conventional waveguides but with a large extended modal area, which releases more
 381 optical mode into the evanescent field. Moreover, as shown in Figure 10b, most of the light is concentrated in
 382 the low-index region which offers direct light-matter contact. Thus, compared to the conventional waveguide,
 383 the sensing performance of an SWG waveguide-based biosensor is highly enhanced.

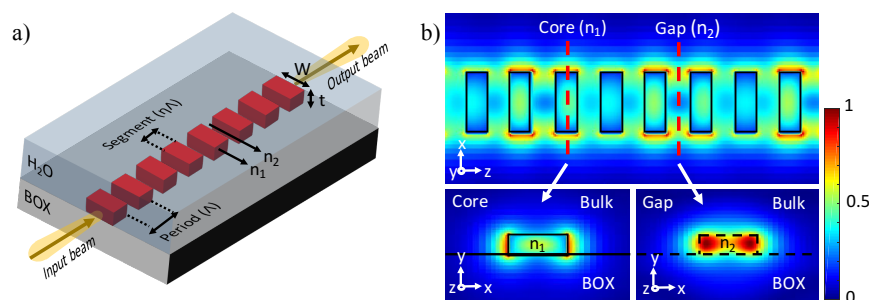


Figure 10. SWG waveguide geometry and simulation results. **(a)** Schematic of an SWG waveguide. W is the waveguide width, t is the thickness, Λ is the SWG period, and η is the duty cycle which determines the length of Si blocks. n_1 and n_2 represent high and low refractive indices. **(b)** The top and cross-sectional views of the electric field intensity distribution of an SWG waveguide. The cross-sections are in the middle of the Si block and gap, respectively.

384 In 2014, Wangüemert-Pérez et al. proposed the application of SWG waveguides for biosensing and
 385 employed a Fourier-type 2D vectorial simulation tool to analyze the sensing performance by varying the duty
 386 cycle, achieving sensitivities of 0.83 RIU/RIU (the change in the n_{eff} of the waveguide mode upon a change
 387 in the RI of the cover) and 1.5×10^{-3} RIU/nm (or for an increase in the thickness of the adsorbed layer) for
 388 bulk and surface sensing [150]. After that, Chen's [151–153] and Chrostowski's [154–157] groups pioneered
 389 the development of SWG waveguide-based biosensors in the SOI platform. Donzella et al. demonstrated
 390 SOI-based SWG optical MRRs for integrated optics and sensing in 2015, showing the first time that SWG-based
 391 resonators with no upper cladding can achieve sensitivities exceeding 383 nm/RIU in water and 270 nm/RIU
 392 in air [154]. A follow-up work was reported by Flueckiger et al. (Figure 11a) by introducing NaCl dilutions and
 393 a typical protein bioassay to the SWG MRR sensor, achieving a bulk sensitivity of 490 nm/RIU with a system
 394 DL of 2×10^{-6} RIU [155]. However, one serious drawback of SWG-based MRR sensors is the relatively low
 395 Q -factor with the upper cladding removed, which is in the range of 1000 ~ 6000 [154]. Trapezoidal silicon
 396 pillars, as reported by Wang et al., can reduce the bend loss by creating an asymmetric effective refractive
 397 index profile in the microring (as shown in Figure 11b), yielding a Q -factor as high as 11500 with a radius of 5
 398 μm , 4.6 times of that (~ 2800) offered by a conventional SWG [151]. By utilizing a trapezoidal-shaped SWG
 399 core, an enhanced sensing capability was analyzed and characterized by Yan et al., obtaining a high Q -factor
 400 of 9100, bulk sensitivity of 440.5 nm/RIU and surface sensitivity of 1 nm/nm with iDL of 3.9×10^{-4} [152]. To
 401 further improve the DL value, Huang et al. theoretically and experimentally optimized an SWG racetrack
 402 resonator in the TM mode to obtain a maximum Q -factor of 9800 and bulk sensitivity of 430 nm/RIU in water,
 403 which corresponds to a 32.5% improved iDL of 3.71×10^{-4} RIU compared to conventional TE-polarized SWG
 404 sensors [153]. Recently, Luan et al. developed two sensitivity enhanced SWG-based multi-box waveguide
 405 biosensors by merging slot and SWG structures, as presented in Figure 11d and 11e [156,157]. The expanded
 406 optical mode and the multiplied surface area for analyte interactions offer a highly improved light-matter
 407 contact at the sensor's surface, thus resulting in a bulk sensitivity of 580 nm/RIU and surface sensitivity of
 408 ~ 1900 pm/nm, respectively [156]. As shown in Figure 11c, SWG waveguides were also integrated into the
 409 MZI-based biosensor as the sensing arm by Sumi et al. in 2017. The device, with the sensing arm's length of
 410 100 μm , is designed to operate at an operating wavelength of 1550 nm in the TE mode with a length-dependent
 411 scalable sensitivity of 931 rad/RIU/mm [158].

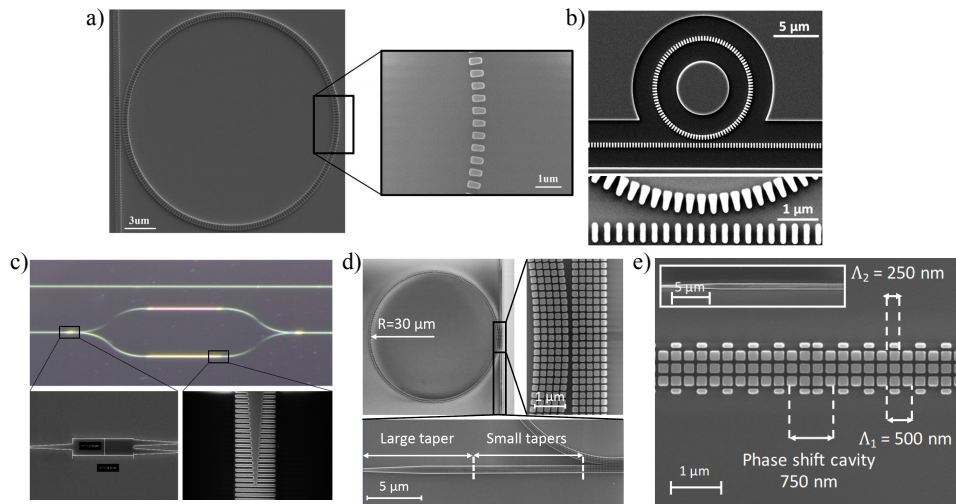


Figure 11. (a) SEM images of a fabricated SWG MRR with waveguide geometry: $W = 500$ nm, $\Lambda = 250$ nm, $t = 220$ nm, and $\eta = 0.7$. Figure adapted with permission from Ref. [155]. (b) SEM images of a $5 \mu\text{m}$ radius trapezoidal silicon pillars based SWG MRR, and a high magnification of the coupling region. Figure adapted with permission from Ref. [151]. (c) Microscopic and SEM images of the fabricated MZI device with an SWG waveguide based sensing arm. Figure adapted with permission from Ref. [158]. (d) SEM images of a multi-box MRR ($r = 30 \mu\text{m}$, $W = 1200$ nm, $t = 220$ nm, $\Lambda = 240$ nm and $\eta = 75\%$) with five rows. Figure adapted with permission from Ref. [156]. (e) SEM images of a 3-row multi-box phase-shifted Bragg grating sensor with 500 nm Bragg period (Λ_1), 250 nm SWG period (Λ_2), and 120 nm wide corrugations. Figure adapted with permission from Ref. [157].

412 3.2.2. Vernier Effect Based Systems

The Vernier effect is a method commonly used in calipers and barometers to enhance the accuracy of instrument measurements by overlapping two scales with different periods, of which one slides along the other one. The overlap between lines of the two scales is used to perform the measurement. Recently, Vernier-principle based sensors have been investigated in the SOI platform by cascading two or more optical devices with different FSR values, where one has the upper cladding removed and represents the RI sensor (as seen in Figure 12a). Due to the different FSRs between the sensing and reference (filter) devices, a spectral response with a major peak plus some minor peaks will be presented at the output. As shown in Figure 12b, the major peaks are located at the overlapped peaks of these devices, showing a Vernier FSR of the least common multiple of total FSR values, and the height of major peaks is determined by the amount of overlap. When the RI above the sensing device changes, the major peak shifts ($\Delta\lambda_{\text{max}}$) discretely which equals to an integer multiple of the reference device's FSR ($\Delta\lambda_{\text{FSR}}^{\text{ref}}$), i.e., $\Delta\lambda_{\text{max}} = m\Delta\lambda_{\text{FSR}}^{\text{ref}}$ [159]. In this way, the Vernier effect cascaded sensor system yields an ultra-high sensitivity which is given by [159]:

$$S = (\lambda_{\text{maj}}/n_{\text{eff}}) \left[\frac{\Delta\lambda_{\text{FSR}}^{\text{ref}}}{(\Delta\lambda_{\text{FSR}}^{\text{ref}} - \Delta\lambda_{\text{FSR}}^{\text{sen}})} \right] = MS_0 \quad (15)$$

413 where λ_{maj} is the wavelength of the major peak, $\Delta\lambda_{\text{FSR}}^{\text{ref}}$ and $\Delta\lambda_{\text{FSR}}^{\text{sen}}$ are the FSRs of reference and sensing
 414 devices respectively, and S_0 is the actual sensitivity of the single sensing device. Thus, the sensitivity of the
 415 optical sensor based on Vernier effect cascaded devices is M times improved than that of a single device,
 416 without requiring a narrow linewidth tunable light source or a high-resolution readout system. The trade off
 417 is that the readout is quantized thus potentially limiting the minimum detection limits.

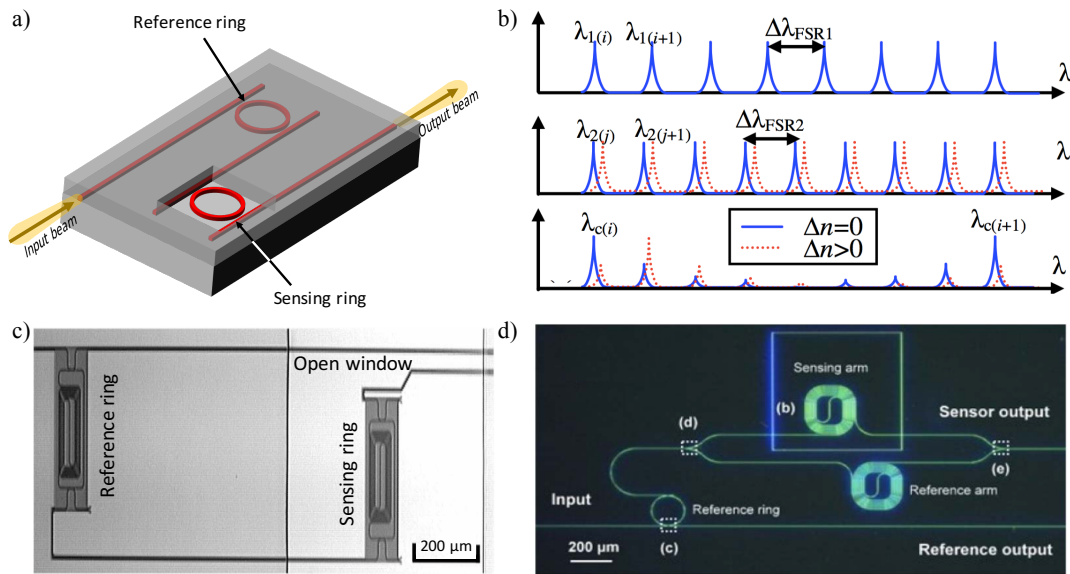


Figure 12. (a) Illustration of the Vernier effect sensing system consisting of two cascaded MRRs with different FSRs. The sensing ring is exposed to RI changes in its environment, while the reference ring is covered by the cladding. (b) Illustrations of calculated transmission spectra of the reference device ($\Delta\lambda_{FSR1}$), sensing device ($\Delta\lambda_{FSR2}$), and cascaded system, respectively. Red-dashed lines represent transmission spectra after an RI change above the sensing device, showing an amplified wavelength shift in the cascaded system. Figure adapted with permission from Ref. [159] (c) Microscopic image of the two cascaded MRRs sensing device fabricated in SOI with an opening at the second MRR. Their footprint is reduced by folding the cavity. Figure adapted with permission from Ref. [160]. (d) Microscopic image of the cascaded MZI and MRR sensor with an opening at the sensing arm of the MZI. Figure adapted with permission from Ref. [161].

418 Earlier, the Vernier principle was applied to the design of integrated tunable lasers [162] and filters
 419 [163,164]. In 2009, Dai et al. proposed a sensing system that consists of two cascaded MRRs, theoretically
 420 showing a two orders higher sensitivity (on the order of 10^5 nm/RIU) than that of a regular single-ring sensor
 421 due to the Vernier effect, and a DL highly related to the FSRs difference [159]. In parallel, He's group pioneered
 422 in investigating cascaded MRR sensors according to the Vernier effect theoretically and experimentally in
 423 the TE [165] and TM [166] modes, yielding sensitivities of 1300 nm/RIU and 24300 nm/RIU, respectively. In
 424 2010, Claes et al. developed cascaded MRRs with very large roundtrip lengths presented in Figure 12c where
 425 FSRs difference is smaller than the FWHM of resonance peaks, and introduced a fitting procedure to reduce
 426 the smallest detectable wavelength shift, obtaining a experimental sensitivity as high as 2169 nm/RIU and
 427 DL , which is no longer limited by the $\Delta\lambda_{FSR}^{ref}$, of 8.3×10^{-6} RIU [160]. One year later, Hu et al. employed a
 428 suspended MRR for sensing by removing the SiO_2 underneath, yielding a sensitivity up to 4.6×10^5 nm/RIU
 429 and DL of 4.8×10^{-6} RIU [167]. In 2012, Passaro et al. introduced a Vernier effect sensing system for gas
 430 detection leveraging slot-waveguide based MRR as the sensing device; a sensitivity of the order of 10^5 nm/RIU
 431 and DL as low as 10^{-5} RIU are achieved for detecting methane and ethane in the air [168]. Moreover, a three
 432 cascaded MRRs sensing system was reported in 2017 by Liu et al. with a high sensitivity of 5866 nm/RIU; the
 433 measurement range which used to be limited by the FSR of the sensing ring obtains a 24.7-fold increment
 434 compared with traditional cascaded MRRs [169].

435 The concept of sensitivity enhancement by employing MZIs to Vernier effect sensing systems was
 436 theoretically demonstrated by La Notte et al., by replacing the sensing MRR with a MZI. The proposed sensor
 437 is considered to reach an ultra-high sensitivity theoretically over 1000 μm /RIU and a very low DL of 10^{-6} RIU
 438 [170]. In 2014, Jiang et al. demonstrated an ultra-high sensitivity Si biosensor based on cascaded MZI and
 439 MRR with the Vernier effect (see Figure 12d). Experimental results indicate a sensitivity of 21500 nm/RIU for
 440 MZI-ring sensor, 7.5 times higher than that (2870 nm/RIU) of a single MZI sensor [161].

441 3.3. Sensitivities Comparison

442 A sensor performance results comparison in the field of silicon photonic biosensors is presented in
443 Table 1 along with different architectures as well as strategies to improve the S and DL values. Due to
444 un-unified units of DL among different articles, bulk sensitivities in the unit of wavelength (or phase) shift per
445 refractive index change are estimated from the results in the publications to serve as a comparison criterion.
446 Moreover, other parameters and performance metrics such as light polarization and wavelength, system and
447 intrinsic detection limits, and Q -factor are also presented.

448 4. Label-Free Detection

449 Generally, two approaches for optical detection are employed by most biosensors: label-based detection
450 and label-free detection. In labeled detection, a label is defined as an additional molecule that is chemically
451 or temporarily attached to the immobilized target to enhance the quantitative signal. Examples include, but
452 are not limited to, a dye molecule (chromophore), a fluorescent tag, or an enzyme. This labeling process
453 can achieve an ultra-low DL (on the order of sub-parts-per-trillion) and provide additional specificity via
454 secondary amplifications [26]. However, it requires sophisticated reagent selection and pairing, in addition to
455 reagent modification including synthesis and purification, which potentially changes intrinsic properties of
456 the capture probe and/or target molecules [173] and dramatically increases the cost and complexity of the
457 assays. Moreover, due to the need for additional steps to perform label-based detection, it is ill-suited for
458 real-time kinetic monitoring. To contrast, label-free detection has emerged as an appealing alternative to
459 labeled detection, utilizing native molecular properties such as molecular weight (MW), RI, and molecular
460 formal charge (FC) for target molecule monitoring. Label-free detection is not without its own drawbacks, as
461 the method is only capable of providing sensitive and specific detection if non-specific binding (NSB) is low,
462 or if the assay has sufficient controls to subtract the contribution of NSB. Additionally, label-free detection
463 requires sufficient signal to be generated upon binding for the sensor to differentiate signal from noise; this
464 can limit label-free detection for certain applications with especially low molecular weight target species, or
465 targets that do not readily interact with specific capture probes/chemistries. Even with these limitations, a
466 large number of biosensors designed for label-free detection have been investigated in the recent research
467 literature [174–176], largely because the method greatly simplifies assays, can reduce both the time and
468 number of steps required, and eliminates experimental uncertainty induced by the labeling process [177].
469 Additionally, label-free detection is highly amenable to the real-time kinetic evaluation of molecular binding
470 and rapid quantification of analytes.

471 Since the first label-free optical biosensor was commercialized in 1990 by Biacore, Inc. [10], an entire
472 field has arisen developing new platforms for label-free biosensing, driven largely by the appeal of addressing
473 the unmet need in medical diagnostics, biosensing, and environmental/biohazard/threat monitoring. Among
474 the new transducers, optical devices based on the SOI platform are among the most promising. Their highly
475 compact footprint, allowing simultaneous multiplexed detection on a single chip, and low fabrication cost in
476 high volumes with CMOS-compatible processes, make them cheap enough to be considered fully disposable.
477 Table 2 gives an overview of a wide variety of exemplary target analytes, arranged in descending molecular
478 weight, that have been detected using label-free SOI-based biosensors, as well as their reported DL s. This
479 survey demonstrates that SOI-based optical biosensors have a wide detection range for analytes with MWs
480 on the order of kilodalton (kDa). For large molecules like micrometer-sized cells and bacteria on the order
481 of megadalton (MDa) or higher, their sizes may exceed the evanescent field range of the sensor and cause
482 a invalid result. For small molecules (normally less than 500 Da), a detectable signal is difficult to achieve,
483 especially for low concentrations, due to the low sensitivity or high noise level of SOI-based sensors.

Table 1. Performance metrics comparison of selected optical biosensors (WG = waveguide, Wvl = wavelength, 1.55 μm where not specified).

Sensor Type	Sensor Configuration	Strategy	Optical Mode	Q-factor ($\times 10^3$)	Bulk Sensitivity (RIU^{-1})	System's Detection Limit (RIU)	Intrinsic Detection Limit (RIU)	
Interferometer	MZI	Vernier	TE	N/A	2.15×10^4 nm	N/A	N/A [161]	
		Suspended	TE	N/A	740 nm	N/A	4×10^{-5} [140]	
	Ring	Slot	TE	N/A	N/A	$1730 \times 2\pi$ rad	1.29×10^{-5}	N/A [128]
		1.31 μm Wvl	TE	N/A	N/A	$540 \times 2\pi$ rad	N/A	N/A [142]
		N/A	TM	N/A	N/A	$460 \times 2\pi$ rad	3.3×10^{-5}	N/A [17]
		N/A	TE	N/A	N/A	$300 \times 2\pi$ rad	N/A	N/A [43]
		Vernier/suspended	TM	N/A	N/A	4.6×10^5 nm	N/A	4.8×10^{-6} [167]
		Vernier	TM	15	2.43×10^4 nm	N/A	N/A [166]	N/A [165]
		Slot/critical coupling	TE	20	1.3×10^3 nm	5.05×10^{-4}	N/A [165]	$< 10^{-4}$ [124]
		Multi-box SWG	TE	6	1.3×10^3 nm	N/A	N/A	1.02×10^{-3} [156]
Microcavity	SWG	TE	2.6	580 nm	N/A	2×10^{-6}	5.5×10^{-4} [155]	
		TE	7	490 nm	N/A	1.59×10^{-2} [122]	N/A [139]	
	Suspended	TE	9.8	429 nm	N/A	N/A	1.2×10^{-3} [19]	
		Thin WG	TE	0.33	298 nm	N/A	N/A	7.5×10^{-4} [19]
	Thin WG	TM	12	290 nm	N/A	N/A	5×10^{-4} [136]	
		TE	4.5	270 nm	N/A	N/A	1.49×10^{-3} [29]	
	Disk	Thin WG	TE	10.1	200 nm	N/A	N/A	3.5×10^{-4} [29]
		1.31 μm Wvl	TE	33.5	113 nm	N/A	N/A	2.7×10^{-3} [29]
	Photonic crystal	Suspended	TE	9.8	91 nm	N/A	N/A	6.8×10^{-4} [21]
			N/A	TE	15	38 nm	N/A	N/A
Suspended		TE	16	142 nm	N/A	N/A	1.8×10^{-3} [21]	
		N/A	TE	0.1	130 nm	8×10^{-4}	N/A	2.07×10^{-5} [132]
2D		Slot	TE	33	26 nm	N/A	N/A	1.88×10^{-2} [80]
		N/A	TE	50	1.5×10^3 nm	7.8×10^{-6}	N/A	8.75×10^{-5} [171]
1D		N/A	TE	0.4	200 nm	2×10^{-3}	N/A	1×10^{-5} [172]
		Ring-slot	TE	11.5	160 nm	N/A	N/A	4×10^{-3} [98]
Bragg grating		Phase-shifted	Slot	TE	174	815 nm	N/A	4×10^{-4} [157]
			N/A	TE	3	130 nm	7×10^{-5}	N/A
	Uniform	Multi-box SWG	TE	6.2	610 nm	N/A	N/A	1.6×10^{-4} [29]
		Slot	TE	15	340 nm	N/A	N/A	9.3×10^{-4} [110]
Uniform	1.31 μm Wvl	TE	76	106 nm	N/A	N/A	N/A [22]	
	N/A	TE	27.6	59 nm	N/A	N/A		
Uniform	N/A	TE	N/A	182 nm	N/A	N/A		

Table 2. Overview of selected biomolecules that have been detected by optical sensors using label-free method (CFU = colony-forming unit, HAU = hemagglutination unit, VP = viral particle).

Biological Material	Target	Weight	Sensor Type	Waveguide Material	Detection Limit
Cell	<i>E. coli</i> O157:H7	1 pg	MRR	Hydex	10 ⁵ CFU/mL [67]
Virus	Avian influenza virus	542 MDa	MZI	Si ₃ N ₄	5 × 10 ⁻⁴ HAU/mL [178]
	Herpes simplex virus	96 MDa	YI	Si ₃ N ₄	850 VP/mL [179]
	Bean pod mottle virus	7 MDa	MRR	Si	1.43 pM [112]
Protein	Human papillomavirus	5 MDa	PhC	Si	1.4 nM [180]
	Immunoglobulin G	150 kDa	PhC	Si	1 ng/mm ² [99]
			MZI	Polymer	3.1 nM [142]
			Vernier MRR	Si	47.3 nM [181]
			MZI	SiO _x N _y	2.14π/nm [182]
			PhC	Si	2.5 fg [25]
			PhC	Si	344 pm/nm [183]
			Slot MZI	Si ₃ N ₄	18 fM [134]
			PhC	Si	49 fM [184]
			MRR	Si	60 fM [71]
			MRR-MZI	Si	20 pM [185]
			MRR	SiO ₂ /Si _x N _y	0.1 nM [61]
			MRR	Si	0.15 nM [18]
			Slot disk	SiN _x	0.55 nM [126]
			Human serum albumins	67 kDa	YI
Prostate specific antigen	28 kDa	MRR	Si	3.4 pg/mm ² [187]	
		MRR	Si	0.4 nM [188]	
		Slot MRR	SiN	1.79 nM [123]	
C-reactive protein	25 kDa	MZI	Si _x N _y	84 fM [189]	
		MRR	Si	0.4 nM [115]	
		MZI	SiN	0.78 nM [190]	
		MRR	Si	53 fM [191]	
		MRR	Si	150 fM [192]	
		Slot MZI	Si ₃ N ₄	1 nM [193]	
Nucleic acid	RNA	7-40 kDa	MZI	Si ₃ N ₄	300 pM [194]
			MZI	Si ₃ N ₄	1 nM [134]
			MRR	Si	1.95 nM [113]
	DNA	7-12 kDa	PhC	Si	19.8 nM [195]
			MRR	Hydex	100 nM [67]
			PhC	Si	0.1 nM [196]
			PhC	Si ₃ N ₄	N/A [197]
Small molecule	Gentamicin	478 Da	PhC	Si	0.1 nM [196]
	biphenyl-4-thiol	186 Da	PhC	Si ₃ N ₄	N/A [197]

484 5. Optical Sensing System Integration

485 To satisfy the need for system operations towards clinical and home healthcare diagnosis, integration
 486 is one of the key challenges to be solved [198]. The SOI platform is appealing since it offers the potential
 487 of optical component integration onto the same substrate. In recent years, massive amount of efforts have
 488 been made to integrate multiple functions to chip-scale silicon PICs, such as on-chip fluidic handling and
 489 optical analysis, as well as data processing [199]. These integrated sensing architectures show the ability
 490 for a high-density, lab-on-a-chip, and portable biosensing platform in the application of POC medical
 491 diagnosis. Here we review research directed towards the integration of microfluidics, lasers, sensing devices
 492 and photodetectors (PDs) on Si substrates for biosensing applications.

493 5.1. Optofluidic Integration

494 Microfluidic systems have been regarded as an essential tool for modern biosensing research due
 495 to outstanding advantages such as low sample consumption, *in-situ* manipulation, short analysis time,
 496 controlled transportation, and high throughput [200,201]. Recently, a synergy technique called optofluidics
 497 has emerged, which integrates microfluidics and photonic architectures to enhance each entity's function
 498 and performance [202]. Introducing optofluidics to silicon photonic biosensing systems not only combines
 499 fluid and light for improved sensing capability and simplification of microsystems but satisfies the function of
 500 on-chip, label-free, real-time detections. In addition, optofluidic sensors are extremely suitable for evanescent

501 field RI detection, since the change of RI scales with the analyte bulk concentration or surface density, rather
502 than the number of molecules in total [202].

503 Polydimethylsiloxane (PDMS) has become the most popular material in the academic microfluidics
504 community since it is inexpensive, easy to fabricate, flexible, optically transparent, and biocompatible
505 [203]. More importantly, PDMS material can be permanently bound to SiO₂ substrates after oxygen plasma
506 treatment [204], which provides a simple and fast approach to build leakage-free microfluidic channels on
507 SOI-based sensors. Many silicon photonic devices including MZIs [96,185], MRRs [156] and PhCs [98,196,201]
508 have employed PDMS microfluidic systems mounted on top as a convenient optofluidic delivery method
509 for analyte detection. However, PDMS also shows some drawbacks. On one hand, PDMS is not suitable for
510 the integration or deposition of electrodes directly on the surface, and has problems such as adsorption of
511 small hydrophobic molecules, swelling in organic solvents, water permeability, and incompatibility under
512 very high-pressure operations [205]. On the other hand, due to the irreversible bonding process, chips are
513 not reusable after mounting the PDMS microfluidic block, and most of the area on the chip only serves as a
514 mechanical support for the fluidic inlet and outlet but not for sensing, which negatively impacts the unit cost
515 [206].

516 Another commercially available material, negative tone photoresist SU-8, has been employed for on-chip
517 optofluidics recently. SU-8 was originally developed as a high-resolution photoresist for the microelectronics
518 industry. Because of its transparency in the near-infrared spectrum and biocompatibility, a thin layer of SU-8
519 coating with microfluidic patterns has been investigated on silicon photonic biosensing systems [44,206],
520 which improves the alignment precision compared to PDMS microfluidics bonding. Furthermore, SU-8
521 can also be used as a cover material for interface passivation of on-chip electrical connections due to
522 its high-resolution patterning and insulation abilities. However, the manufacturing process of the SU-8
523 microfluid requires the use of clean room facility equipment involving complex and numerous processing
524 steps, which hinders mass production at a low price. In addition, variation in conditions such as humidity and
525 SU-8 composition may affect fabrication protocols, contributing to batch-to-batch variability [207]. Other
526 materials such as glass [208], polycarbonate (PC) [209], cyclic olefin copolymer (COC) [210] and epoxy [211]
527 were also reported for the on-chip optofluidic integration.

528 Digital microfluidics is an emerging technology in the field of biosensing by using microdroplets instead
529 of continuous flows. Drops the size of microliter or picoliter can be generated, transported, mixed, and
530 split in miniaturized reaction chambers without moving equipment such as pumps or valves, which offers
531 great potential for pump-free high-throughput liquid handling and avoids on-chip cross-contaminations
532 [212]. Electrowetting is the most commonly used technique for microdroplet actuation, which refers to
533 electric field-induced interfacial tension changes between the liquid and the dielectric layer, resulting in a
534 contact angle change, and thus droplet movement [213]. The integration of SOI-based optical sensors and
535 digital microfluidics has been demonstrated by utilizing MRRs [212,214] and microdisks [215] since 2008,
536 showing comparable sensitivities to their counterparts measured in standard optofluidic systems. Another
537 approach for eliminating pumps and valves has been investigated recently by employing an integrated,
538 microtechnological pumping method. The actuation principle is mainly based on the deflection of a
539 deformable polymer membrane to push the liquid from the reservoir towards the microfluidic channel,
540 where the deflection results from the increased pressure underneath the membrane by the electrolytically
541 generated gas [216]. Geidel et al. showed an integrated microfluidic design consisting of multiple reservoirs
542 and electrochemical pumps for time-controlled delivery, which has been tested and validated by SiN-based
543 MRR biosensors, indicating the possibility of on-chip liquid handling integration for high-level miniaturized
544 optical biosensors [209]. However, the prototype worked with a low sensitivity due to the unselective binding
545 within the cartridge or selective binding exceeding the evanescent field on the MRR, which requires further
546 optimizations for the surface biofunctionalization.

547 5.2. Optoelectronic Integration

548 One of the biggest roadblocks towards the large-scale commercialization of photonic biosensors is the
549 low-cost high-yield integration of light sources to operate reliably whilst consuming minimal power. These

550 goals are usually traded-off against each other with the choice of platform for integrating the light source,
551 the sensor device, and the photodetector (PD) to achieve a complete lab-on-a-chip system. For instance,
552 to benefit from a high-yield and low-cost production, leveraging existing CMOS fabs seems to be the ideal
553 solution. This requires the integration of these three elements on a single Si CMOS-compatible die. However,
554 integrating the active laser source with the passive sensor device and the PD remains a challenge. Several
555 techniques utilized for the chip-scale optoelectronic integration are presented below, and advantages brought
556 as well as challenges faced by each method are highlighted.

557 5.2.1. On-Chip Lasers

558 Driven by the promises lasers on Si hold for optical communication [217], several groups across the world
559 have demonstrated integrated lasers on Si dies implemented using either group IV materials (Si or Ge) or group
560 III/V compounds [218]. While using group IV elements seem to be an appealing and practical solution in terms
561 of cost and portability, existing methods using Si cannot yet render an electrical I/O-based lab-on-a-chip
562 because they rely on optical pumping mechanisms [219,220], making it an unattractive solution at the
563 moment. Electrically-pumped Ge lasers integrated on Si, however, have been demonstrated [221]. Despite its
564 indirect bandgap, straining and n-doping Ge can tailor its bandgap to make it direct [222]. Repercussions of
565 this approach are high threshold currents [221] thus increasing the total power budget of the biosensors.

566 On the other hand, III/V lasers integrated on Si have been demonstrated with a much higher efficiency
567 in comparison to Ge, thanks to their direct bandgap and superior gain characteristics. While monolithic
568 integration of III/V compounds on Si seems to be the optimum solution for ease of portability and highest
569 density integration, the biggest bottleneck towards the direct monolithic growth of III/V compounds on Si lies
570 in the lattice and thermal expansion coefficient mismatch between the Si material and III/V compounds [218].
571 To solve this problem, three main approaches have been demonstrated to integrate III/V lasers on Si chips:
572 (1) direct mounting, (2) hybrid approaches through direct and indirect bonding heterogeneous integration,
573 and (3) monolithic integration using sophisticated growth techniques.

574 Direct mounting includes flip-chip bonding using solder bumps through edge-coupled III/V to Si
575 waveguides [223–225] or through vertical coupling using SiO₂-SiO₂ bonding techniques [226,227]. The main
576 advantage this method brings is the independent growth of III/V materials on its native substrate, thus
577 benefiting from the merits of a III/V compound as a gain medium. In addition, the solder bumps provide
578 a means to dissipate the generated heat from the III/V die to the Si substrate leveraging its high thermal
579 conductivity [228]. Furthermore, with a rigorous design of spot-size convertors and accurate alignment,
580 high wall-plug efficiency (WPE, the ratio of the output optical to input electrical power), up to 35% [229]
581 can be achieved. The laser's cavity can be shared between the III/V gain chip and Si, known as external
582 cavity lasers (ECLs). ECLs allow for the independent control over the laser's properties such as the linewidth
583 [230], wavelength tuning [231], and stabilization using on-Si chip electrical control [72,232,233]. Nevertheless,
584 common issues of direct mounting integration include low efficient end-coupling between the III/V and Si
585 waveguides requiring precise alignment, and degradation in the laser's overall performance due to possible
586 back reflections into the laser source [234]. Even if aligned at the microscale, the process is both costly and
587 tedious [228] which adds to the overall cost of a lab-on-a-chip system making it an expensive solution and
588 limiting its usage for prototyping purposes.

589 An alternative and more efficient way of integrating III/V gain materials on Si substrates is through
590 indirect (using metal or polymer layers) or direct bonding techniques [218,235], commonly referred to as
591 hybrid or heterogeneous integration. The biggest advantage of heterogeneous integration above direct
592 mounting is that it does not require the precise alignment at the microscale, since the III/V active layers
593 are lithographically aligned with high precision. Direct bonding can be achieved using Oxygen plasma
594 at low temperatures. This was first demonstrated by Bowers et al. [236,237], and due to it being a
595 cost-effective solution, this work resulted in a startup, Aurrion Inc. that was later acquired by Juniper
596 Networks [238,239]. Direct bonding has the advantage of not requiring the addition of any extra layers, and
597 lasers formed this way can achieve low threshold currents [218]. Indirect bonding, on the other hand, was
598 demonstrated using metal-assisted adhesive bonding [240–242], whereas others have used polymers such as

divinylsiloxane-bis-benzocyclobutene (DVS-BCB) [235,243,244]. While metals provide better heat dissipation due to their high thermal conductivity, polymers are more straightforward to fabricate and unlike metals, do not absorb light. Polymers, however, have the disadvantage of having a high thermal resistance thus localizing heat. To mitigate its effects, Roelkens has fabricated polymers with < 50 nm thickness, thus reducing its effect in localizing the heat [235]. The same group have extended this technique and demonstrated light sources at a various wavelength for biosensing applications [245]. This makes heterogeneous integration a scalable technique that enables dense integration of III/V in SOI platforms, thus reducing the potential costs of a lab-on-a-chip system. Furthermore, ECLs can be implemented in the hybrid approach, thus leveraging the merits that ECLs brings [231].

There are several monolithic approaches for integrating III/V lasers and active devices on Si substrates. Epitaxial layer overgrowth (ELOG) is one way to overcome the formation of threading dislocations that arise due to the lattice and thermal expansion mismatch between III/V and Si materials [246]. The process is yet more complicated in comparison to the formerly mentioned techniques.

While the choice of III/V integration method on Si directly influence the overall laser's performance, the choice of the III/V active gain medium physical structure is equally important. For instance, to achieve a low-power and reliable (avoiding overheating) operation, the WPE of the laser should be maximized. The WPE or the conversion efficiency is a crucial figure of merit in a laser design, which is dependent upon the threshold current, electron density and the internal losses in the laser's cavity. These parameters are dependent upon the band structure of the chosen active gain medium, which is engineered by physically restricting the electrons motion to form double heterostructure (DH), quantum well (QW), quantum wire (QWR) or quantum dot (QD) structures. Among the various structures reported, QDs stand out as they offer superior properties compared to their counterparts DHs, QWs, or QWRs as shown in Figure 13. Thanks to the tight electron confinement, thus increasing the optical gain dependence on the current density, which reduces the transparency current and makes the threshold current density temperature insensitive [247]. Motivated by lowering the threshold current and making a temperature insensitive laser, Dingle and Henry proposed the QD laser back in 1976 [248]. Since its analysis by Arakawa and Sakaki in 1982 [249], a plethora of applications on-Si platform has leveraged the merits QD lasers brought [250–253]. Perhaps, one of the main reasons behind the proliferation of QDs lies in its minimal sensitivity to defects [254], which drew increased attention and allowed for the growth of III/V QDs on Si [255]. This is very promising, however, its compatibility with CMOS processes remains controversial [72]. Recently, researchers at University College London [256] demonstrated electrically pumped III/V QD lasers on Si with superior characteristics, such as a low threshold current density of 62.5 A/cm², room temperature output power of > 105 mW, and over several months of reliable continuous operation, giving an estimated failure of over ten years of operation. This holds great promises towards the high-volume practical realization of low-cost photonic biosensors.

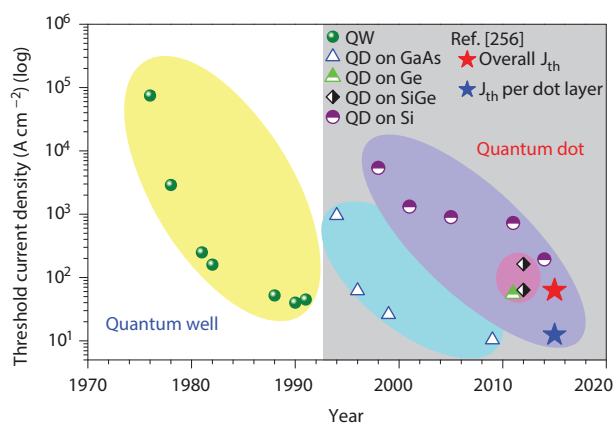


Figure 13. Historical development of low-dimensional heterostructure lasers, showing the record threshold current densities. The blue and red stars indicate the threshold values achieved in Ref. [256] for a single and multiple QD layers, respectively. Figure adapted with permission from Ref. [256].

633 5.2.2. On-Chip Detectors

634 For a lab-on-a-chip system with electrical I/Os, an on-chip photodetector is required to convert the light
635 signal for further processing. There are several on-Si PDs implemented either using III/V compounds, or
636 using group IV elements such as Si or Ge. The choice of PDs depends on the detection wavelength of interest.
637 Wang et al. have heterogeneously integrated III/V PDs on Si substrate for operation at a wavelength of 2 μm
638 [245]. Other techniques explored include thermo-electric PDs [245,257]. However, across the C-band, besides
639 III/V compounds [235], Ge and Si could be used for photodetection. The main advantages of using Si or Ge is
640 their ease of fabrication with a CMOS fab. Despite Si's transparency at the C-band, doping Si can increase
641 the Si waveguide's sensitivity to incoming light across the C-band either due to surface states [258], or due to
642 the introduction of mid-band-gap defect states [258–261]. Si-based defect-mediated PDs, however, suffer
643 from either low responsivities or large photoconductive gain at the expense of a much larger dark current
644 [260], which is undesirable for biosensing applications. Ge-based PDs, however, have superior characteristics.
645 Recent results showed Ge on Si PDs with a high responsivity of 0.74 A/W and low dark currents of less than 4
646 nA [262]. Their integration into an on-chip biosensor was also demonstrated in Ref [206], and its performance
647 was analyzed. These characteristics make Ge-based PDs ideal for biosensing at a wavelength of 1.3 μm or
648 1.5 μm in the SOI platform.

649 5.3. Readout

650 For conventional evanescent field biosensing techniques, two methods are usually employed for
651 the quantitative detection of analytes at the sensor's surface in real-time: the first one is monitoring the
652 wavelength (or phase) shift in the transmission spectrum through scanning the input light source wavelength,
653 which allows a large dynamic range for sensors; the other one is detecting the transmission intensity change
654 caused by shifts at a fixed wavelength and providing precise detection with a very small concentration of
655 analytes [263,264]. Both of these spectral domain approaches require precise optical spectrum scanning and
656 processing systems, such as a wavelength-tunable laser and high-resolution photodetectors. Correspondingly,
657 two types of noise sources, wavelength noise and intensity noise, are categorized based on different
658 sensing techniques. Wavelength noise is mainly generated from the light source wavelength shift and
659 thermally influenced fluctuations of the sensor, whereas the intensity noise is caused by light source intensity
660 fluctuations, the variation of input coupling, and PD noise [265]. Optical spectrum curving fitting is a powerful
661 tool to enhance the wavelength resolution. Taking into account of the entire spectrum, a fitting process
662 can improve the eventual signal-to-noise ratio (SNR) by \sqrt{N} , where N is the total number of data points in
663 the spectrum [28]. By applying this algorithm to silicon photonic biosensors, a wavelength measurement
664 precision much smaller than both the light source linewidth and the peak FWHM is achieved [265], with a
665 factor of approximately 10 to 10^3 [58]. Therefore, the system's DL with an improved linewidth in the spectrum
666 readout can greatly enhance sensor performance as compared to the intrinsic DL using the peak linewidth
667 according to Equation 5 and 12.

668 Recently, Wang et al. proposed a biosensing scheme using a coupled-resonator optical-waveguide
669 (CROW) in the SOI platform, where a series of coupled MRRs cause a specific spatial domain scattering
670 pattern by applying a fixed wavelength to excites the CROW [263]. Based on the captured intensity of the
671 light-scattering of each MRR, the whole structure intensity pattern dependent on the RI change above the
672 CROW is presented as the readout scheme by the imaging camera. By introducing different concentrations of
673 NaCl solutions to an 8-MRR CROW sensor, a bulk sensitivity of $\sim 752 \text{ RIU}^{-1}$ and DL of $\sim 6 \times 10^{-6} \text{ RIU}$ are
674 achieved [263]. Although no spectrum scanning system is needed in this design for the sensor's excitation
675 and detection, the simultaneous imaging system still impedes the goal of the low cost, portable development.

676 5.4. State-Of-The-Art CMOS-Chip Packaging

677 Compared to traditional benchtop sensors and instrumentation, biosensors that rely on CMOS processes
678 offer lower cost, lower power and smaller size with a high-density on-chip sensing array [266]. In terms
679 of lab-on-a-chip monitoring, the primary challenge is the integration of sensing arrays interfaced with

680 fluid samples and electrical interconnects for data processing on CMOS substrates. Furthermore, die-level
 681 CMOS substrates are always millimeter-sized which obstructs the on-chip microfluidics and electrical
 682 interconnections integration for high-throughput.

683 To overcome these difficulties, several post-CMOS approaches have been investigated as system-level
 684 packaging to implement electronic and biological detection functions. Fluid barrier materials, such as
 685 PDMS, epoxy, SU-8, oxide/nitride, and parylene, have been employed for integrating CMOS chips with
 686 microfluidics. Li et al. reported a chip-in-package process utilizing wire bonding technology for the die-level
 687 on-CMOS biosensor integration [267]. By depositing a 2- μm -thick parylene layer as the insulating coating,
 688 the biosensor is enabled for operations in liquid with a good functionality of CMOS electronics [267]. Huang
 689 et al. developed a lab-on-CMOS platform for electrochemical microsystems by using oxide/nitride/oxide
 690 (ONO) passivation layers, which allows the functional integrity of multi-channel microfluidic structures
 691 and on-CMOS electrodes [268]. For the size disparity between the CMOS chip and on-chip microfluidics,
 692 die-level CMOS chips have been encapsulated into a substrate carrier which enlarges the surface area for
 693 further processes. In 2014, Datta-Chaudhuri et al. presented a simple packaging method for die-level
 694 CMOS foundry-fabricated chips, which are embedded in epoxy handle wafer for a level, enlarged surface,
 695 allowing subsequent post-processing and microfluidic integration [269]. Parylene-C was selectively exposed
 696 to the surface for the passivation of electrical connections. As shown in Figure 14a, due to the flat surface
 697 around the chip, good electrical continuity of fan-out metal traces from the chip to the edge of the wafer
 698 is achieved, enabling the subsequent off-chip data communication [269]. Similar approaches have been
 699 considered for PICs. Laplatine et al. developed a novel system-level architecture by embedding the individual
 700 photonic-electronic die into a 2-inch epoxy wafer, with electrical interconnects and microfluidic channels
 701 based on a lab-scale Fan-Out Wafer-Level-Packaging process (FOWLP) presented in Figure 14b [206]. SU-8
 702 was selected for the microfluidic channels patterning as well as electrical connections passivation. By
 703 characterizing on-chip Ge PD components in the photovoltaic mode, they demonstrated an approach for
 704 biomolecule detections even with a low optical power [206]. In addition, sensor performance was also
 705 characterized by introducing standard NaCl solutions and bio-sandwich assays to FOWLP-packaged chips. A
 706 bulk sensitivity of 220 nm/RIU is achieved, close to the sensing capability of the passive counterpart [270].
 707 Similarly, a CMOS-compatible epoxy chip-in-carrier process was developed by Lin et al. [271]. By introducing
 708 a planar screen-printed silver ink metallization technique with mounted multichannel PDMS microfluidics on
 709 the device's surface, electrochemical and microfluidic experiments were evaluated by interconnect resistance
 710 measurements, showing high effectiveness for lab-on-CMOS applications to achieve desired capability with
 711 high yield and low material and tool cost [271].

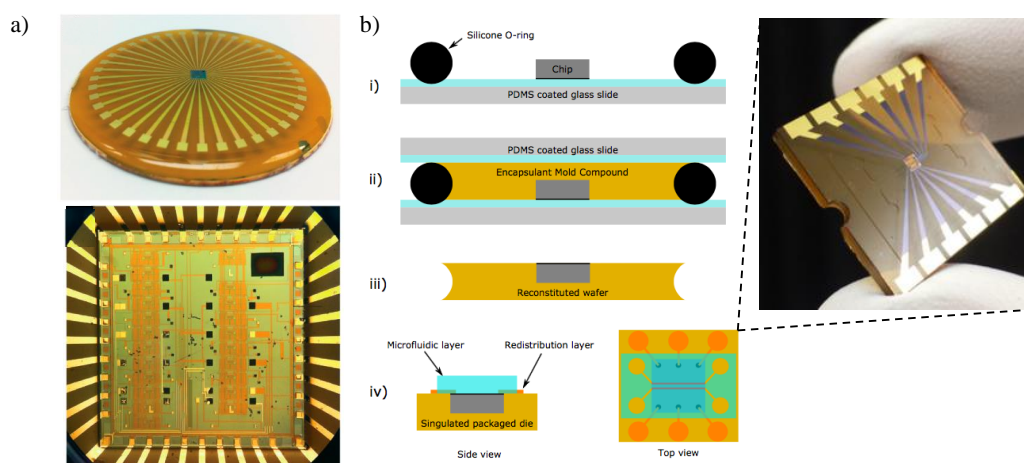


Figure 14. (a) Images of the die-embedded epoxy handle wafer with thin-film Au connections fan-out from the chip to the edge, and close-up view around the die. Figure adapted with permission from Ref. [269]. (b) Schematic of lab-scale FOWLP, and image of the $16 \times 16 \text{ mm}^2$ packaged CMOS die after singulation. Figure adapted with permission from Ref. [206].

712 6. Conclusions

713 Over the past two decades, silicon photonics technology has attracted enormous attention and research
714 effort in optoelectronic integration to impact multiple application areas. Leveraging the mature CMOS
715 manufacturing technology, Si-based optical biosensing platforms have experienced huge breakthroughs
716 in chip-scale integration and miniaturization for hand-held, label-free bio-diagnosis with high-volume
717 production at low cost. By monitoring perturbations of the guided light in the waveguide, target molecules
718 that change the RI in the vicinity of the sensor can be detected in real-time, showing a significant sensing
719 capability down to sub-femtomolar. Moreover, some of the Si-based biosensing architectures have even been
720 commercialized for label-free detection by companies such as Axela, Inc., Corning, Inc., and Genalyte, Inc.,
721 through employing optical gratings, microplates, and microresonators into the sensing platform. However,
722 due to the challenge of the monolithic integration on Si substrate, achieving a complete chip-scale integration
723 of the portable biosensing platform for POC diagnosis requires further development. Compared to very
724 commercially-mature label-free biosensing technique, i.e., SPR, the Si-based sensing approach still needs an
725 improvement in sensitivity for label-free detection of small molecule analytes to fulfill the market demand.
726 Thanks to the intensive research effort throughout the world, we firmly believe that true lab-on-a-chip,
727 portable biosensing devices will be realized and revolutionize global healthcare.

728 **Acknowledgments:** The authors would like to acknowledge support from the CMC Microsystems, Natural Sciences and
729 Engineering Research Council of Canada (NSERC), MITACS Accelerate program, and NSERC CREATE Silicon Electronic
730 Photonic Integrated Circuits (SEPIC) research training program. Enxiao Luan received the support from the China
731 Scholarship Council (CSC) for four years study at the University of British Columbia.

732 **Conflicts of Interest:** The authors declare no conflict of interest.

733 References

- 734 1. Wulfschuhle, J.D.; Liotta, L.A.; Petricoin, E.F. Early detection: proteomic applications for the early detection of cancer.
735 *Nature reviews cancer* **2003**, *3*, 267.
- 736 2. McDermott, U.; Downing, J.R.; Stratton, M.R. Genomics and the continuum of cancer care. *New England Journal*
737 *of Medicine* **2011**, *364*, 340–350.
- 738 3. Snyder, E.L.; Stramer, S.L.; Benjamin, R.J. The safety of the blood supply—time to raise the bar. *N Engl J Med* **2015**,
739 *372*, 1882–1885.
- 740 4. Dhawan, A.P.; Heetderks, W.J.; Pavel, M.; Acharya, S.; Akay, M.; Mairal, A.; Wheeler, B.; Dacso, C.C.; Sunder, T.;
741 Lovell, N.; others. Current and future challenges in point-of-care technologies: A paradigm-shift in affordable
742 global healthcare with personalized and preventive medicine. *IEEE journal of translational engineering in health*
743 *and medicine* **2015**, *3*, 1–10.
- 744 5. Yager, P.; Domingo, G.J.; Gerdes, J. Point-of-care diagnostics for global health. *Annu. Rev. Biomed. Eng.* **2008**,
745 *10*, 107–144.
- 746 6. Arlett, J.; Myers, E.; Roukes, M. Comparative advantages of mechanical biosensors. *Nature nanotechnology* **2011**,
747 *6*, 203.
- 748 7. Mascini, M.; Tombelli, S. Biosensors for biomarkers in medical diagnostics. *Biomarkers* **2008**, *13*, 637–657.
- 749 8. Clark, L. Monitor and control of blood and tissue oxygen tensions: Transactions of the American Society for
750 Artificial Internal Organs, v. 2 **1956**.
- 751 9. At, J. Business Prospects and Future Scope of Biosensors Market in Medical Device Industry.
752 [http://prsync.com/grand-view-research-inc/business-prospects-and-future-scope-of-biosensors-market-in-](http://prsync.com/grand-view-research-inc/business-prospects-and-future-scope-of-biosensors-market-in-medical-device-industry-1211986/)
753 [medical-device-industry-1211986/](http://prsync.com/grand-view-research-inc/business-prospects-and-future-scope-of-biosensors-market-in-medical-device-industry-1211986/), 2016. Accessed: 2018-4-24.
- 754 10. Lechuga, L.M. Optical biosensors. *Comprehensive analytical chemistry* **2005**, *44*, 209–250.
- 755 11. Washburn, A.L.; Gunn, L.C.; Bailey, R.C. Label-free quantitation of a cancer biomarker in complex media using
756 silicon photonic microring resonators. *Analytical chemistry* **2009**, *81*, 9499–9506.
- 757 12. Zinoviev, K.; Carrascosa, L.G.; Sánchez del Río, J.; Sepúlveda, B.; Domínguez, C.; Lechuga, L.M. Silicon photonic
758 biosensors for lab-on-a-chip applications. *Advances in Optical Technologies* **2008**, *2008*.
- 759 13. Soref, R. The past, present, and future of silicon photonics. *IEEE Journal of selected topics in quantum electronics*
760 **2006**, *12*, 1678–1687.

- 761 14. Bogaerts, W.; De Heyn, P.; Van Vaerenbergh, T.; De Vos, K.; Kumar Selvaraja, S.; Claes, T.; Dumon, P.; Bienstman, P.;
762 Van Thourhout, D.; Baets, R. Silicon microring resonators. *Laser & Photonics Reviews* **2012**, *6*, 47–73.
- 763 15. Fan, X.; White, I.M.; Shopova, S.I.; Zhu, H.; Suter, J.D.; Sun, Y. Sensitive optical biosensors for unlabeled targets: A
764 review. *analytica chimica acta* **2008**, *620*, 8–26.
- 765 16. Schipper, E.; Brugman, A.; Dominguez, C.; Lechuga, L.; Kooyman, R.; Greve, J. The realization of an integrated
766 Mach-Zehnder waveguide immunosensor in silicon technology. *Sensors and Actuators B: Chemical* **1997**,
767 *40*, 147–153.
- 768 17. Densmore, A.; Xu, D.X.; Janz, S.; Waldron, P.; Mischki, T.; Lopinski, G.; Delège, A.; Lapointe, J.; Cheben,
769 P.; Lamontagne, B.; others. Spiral-path high-sensitivity silicon photonic wire molecular sensor with
770 temperature-independent response. *Optics letters* **2008**, *33*, 596–598.
- 771 18. De Vos, K.; Bartolozzi, I.; Schacht, E.; Bienstman, P.; Baets, R. Silicon-on-Insulator microring resonator for sensitive
772 and label-free biosensing. *Optics express* **2007**, *15*, 7610–7615.
- 773 19. Talebifard, S.; Schmidt, S.; Shi, W.; Wu, W.; Jaeger, N.A.; Kwok, E.; Ratner, D.M.; Chrostowski, L. Optimized sensitivity
774 of Silicon-on-Insulator (SOI) strip waveguide resonator sensor. *Biomedical optics express* **2017**, *8*, 500–511.
- 775 20. Armani, A.M.; Kulkarni, R.P.; Fraser, S.E.; Flagan, R.C.; Vahala, K.J. Label-free, single-molecule detection with
776 optical microcavities. *science* **2007**, *317*, 783–787.
- 777 21. Grist, S.M.; Schmidt, S.A.; Flueckiger, J.; Donzella, V.; Shi, W.; Fard, S.T.; Kirk, J.T.; Ratner, D.M.; Cheung,
778 K.C.; Chrostowski, L. Silicon photonic micro-disk resonators for label-free biosensing. *Optics express* **2013**,
779 *21*, 7994–8006.
- 780 22. Jugessur, A.; Dou, J.; Aitchison, J.; De La Rue, R.; Gnan, M. A photonic nano-Bragg grating device integrated with
781 microfluidic channels for bio-sensing applications. *Microelectronic Engineering* **2009**, *86*, 1488–1490.
- 782 23. Prabhathan, P.; Murukeshan, V.; Jing, Z.; Ramana, P.V. Compact SOI nanowire refractive index sensor using phase
783 shifted Bragg grating. *Optics express* **2009**, *17*, 15330–15341.
- 784 24. Mandal, S.; Serey, X.; Erickson, D. Nanomanipulation using silicon photonic crystal resonators. *Nano letters* **2009**,
785 *10*, 99–104.
- 786 25. Lee, M.; Fauchet, P.M. Two-dimensional silicon photonic crystal based biosensing platform for protein detection.
787 *Optics express* **2007**, *15*, 4530–4535.
- 788 26. Schmidt, S. Enhancing the performance of silicon photonic biosensors for clinical applications. PhD thesis,
789 University of Washington, 2017.
- 790 27. Washburn, A.L.; Bailey, R.C. Photonics-on-a-chip: recent advances in integrated waveguides as enabling detection
791 elements for real-world, lab-on-a-chip biosensing applications. *Analyst* **2011**, *136*, 227–236.
- 792 28. Chrostowski, L.; Grist, S.; Flueckiger, J.; Shi, W.; Wang, X.; Ouellet, E.; Yun, H.; Webb, M.; Nie, B.; Liang, Z.; others.
793 Silicon photonic resonator sensors and devices. *Laser Resonators, Microresonators, and Beam Control XIV*.
794 International Society for Optics and Photonics, 2012, Vol. 8236, p. 823620.
- 795 29. Schmidt, S.; Flueckiger, J.; Wu, W.; Grist, S.M.; Fard, S.T.; Donzella, V.; Khumwan, P.; Thompson, E.R.; Wang, Q.;
796 Kulik, P.; others. Improving the performance of silicon photonic rings, disks, and Bragg gratings for use in label-free
797 biosensing. *Biosensing and Nanomedicine VII*. International Society for Optics and Photonics, 2014, Vol. 9166, p.
798 91660M.
- 799 30. Kozma, P.; Kehl, E.; Ehrentreich-Förster, E.; Stamm, C.; Bier, F.F. Integrated planar optical waveguide interferometer
800 biosensors: A comparative review. *Biosensors and Bioelectronics* **2014**, *58*, 287–307.
- 801 31. Fernández Gavela, A.; Grajales García, D.; Ramirez, J.C.; Lechuga, L.M. Last advances in silicon-based optical
802 biosensors. *Sensors* **2016**, *16*, 285.
- 803 32. Young, T. I. The Bakerian Lecture. Experiments and calculations relative to physical optics. *Philosophical*
804 *transactions of the Royal Society of London* **1804**, *94*, 1–16.
- 805 33. Zehnder, L. *Ein neuer interferenzrefraktor*; Springer, 1891.
- 806 34. Mach, L. Ueber einen interferenzrefraktor. *Zeitschrift für Instrumentenkunde* **1892**, *12*, 89.
- 807 35. Jenkins, E.; White, H. Fundamentals of Optics. MacGraw Hill Book Company. *New York* **1957**, pp. 211–231.
- 808 36. Jenkins, E.; White, H. The Double Slit. MacGraw Hill Book Company. *New York* **1957**, pp. 311–327.
- 809 37. Estevez, M.C.; Alvarez, M.; Lechuga, L.M. Integrated optical devices for lab-on-a-chip biosensing applications.
810 *Laser & Photonics Reviews* **2012**, *6*, 463–487.
- 811 38. Dante, S.; Duval, D.; Sepúlveda, B.; González-Guerrero, A.B.; Sendra, J.R.; Lechuga, L.M. All-optical phase
812 modulation for integrated interferometric biosensors. *Optics express* **2012**, *20*, 7195–7205.

- 813 39. Heideman, R.; Kooyman, R.; Greve, J. Development of an optical waveguide interferometric immunosensor. *Sensors and Actuators B: Chemical* **1991**, *4*, 297–299.
- 814
- 815 40. Heideman, R.; Kooyman, R.; Greve, J. Performance of a highly sensitive optical waveguide Mach-Zehnder
816 interferometer immunosensor. *Sensors and Actuators B: Chemical* **1993**, *10*, 209–217.
- 817 41. Heideman, R.; Lambek, P. Remote opto-chemical sensing with extreme sensitivity: design, fabrication and
818 performance of a pigtailed integrated optical phase-modulated Mach-Zehnder interferometer system. *Sensors
819 and Actuators B: Chemical* **1999**, *61*, 100–127.
- 820 42. Crespi, A.; Gu, Y.; Ngamsom, B.; Hoekstra, H.J.; Dongre, C.; Pollnau, M.; Ramponi, R.; van den Vlekkert, H.H.;
821 Watts, P.; Cerullo, G.; others. Three-dimensional Mach-Zehnder interferometer in a microfluidic chip for
822 spatially-resolved label-free detection. *Lab on a Chip* **2010**, *10*, 1167–1173.
- 823 43. Densmore, A.; Xu, D.X.; Waldron, P.; Janz, S.; Cheben, P.; Lapointe, J.; Delge, A.; Lamontagne, B.; Schmid, J.; Post,
824 E. A silicon-on-insulator photonic wire based evanescent field sensor. *IEEE Photonics Technology Letters* **2006**,
825 *18*, 2520–2522.
- 826 44. Densmore, A.; Vachon, M.; Xu, D.X.; Janz, S.; Ma, R.; Li, Y.H.; Lopinski, G.; Delâge, A.; Lapointe, J.; Luebbert, C.;
827 others. Silicon photonic wire biosensor array for multiplexed real-time and label-free molecular detection. *Optics
828 letters* **2009**, *34*, 3598–3600.
- 829 45. Shew, B.; Cheng, Y.; Tsai, Y. Monolithic SU-8 micro-interferometer for biochemical detections. *Sensors and
830 Actuators A: Physical* **2008**, *141*, 299–306.
- 831 46. Mathesz, A.; Fábíán, L.; Valkai, S.; Alexandre, D.; Marques, P.V.; Ormos, P.; Wolff, E.K.; Dér, A. High-speed integrated
832 optical logic based on the protein bacteriorhodopsin. *Biosensors and Bioelectronics* **2013**, *46*, 48–52.
- 833 47. Dumais, P.; Callender, C.L.; Noad, J.P.; Ledderhof, C.J. Integrated optical sensor using a liquid-core waveguide in a
834 Mach-Zehnder interferometer. *Optics express* **2008**, *16*, 18164–18172.
- 835 48. Brandenburg, A.; Henninger, R. Integrated optical Young interferometer. *Applied optics* **1994**, *33*, 5941–5947.
- 836 49. Brandenburg, A. Differential refractometry by an integrated-optical Young interferometer. *Sensors and Actuators
837 B: Chemical* **1997**, *39*, 266–271.
- 838 50. Brandenburg, A.; Krauter, R.; Künzel, C.; Stefan, M.; Schulte, H. Interferometric sensor for detection of
839 surface-bound bioreactions. *Applied Optics* **2000**, *39*, 6396–6405.
- 840 51. Schmitt, K.; Schirmer, B.; Hoffmann, C.; Brandenburg, A.; Meyrueis, P. Interferometric biosensor based on
841 planar optical waveguide sensor chips for label-free detection of surface bound bioreactions. *Biosensors and
842 Bioelectronics* **2007**, *22*, 2591–2597.
- 843 52. Wang, M.; Uusitalo, S.; Liedert, C.; Hiltunen, J.; Hakalahti, L.; Myllylä, R. Polymeric dual-slab waveguide
844 interferometer for biochemical sensing applications. *Applied optics* **2012**, *51*, 1886–1893.
- 845 53. Hiltunen, M.; Hiltunen, J.; Stenberg, P.; Aikio, S.; Kurki, L.; Vahimaa, P.; Karioja, P. Polymeric slot waveguide
846 interferometer for sensor applications. *Optics Express* **2014**, *22*, 7229–7237.
- 847 54. Zinoviev, K.E.; González-Guerrero, A.B.; Domínguez, C.; Lechuga, L.M. Integrated bimodal waveguide
848 interferometric biosensor for label-free analysis. *Journal of Lightwave Technology* **2011**, *29*, 1926–1930.
- 849 55. Duval, D.; González-Guerrero, A.B.; Dante, S.; Osmond, J.; Monge, R.; Fernández, L.J.; Zinoviev, K.E.; Domínguez,
850 C.; Lechuga, L.M. Nanophotonic lab-on-a-chip platforms including novel bimodal interferometers, microfluidics
851 and grating couplers. *Lab on a Chip* **2012**, *12*, 1987–1994.
- 852 56. White, I.M.; Fan, X. On the performance quantification of resonant refractive index sensors. *Optics express* **2008**,
853 *16*, 1020–1028.
- 854 57. Flueckiger, J. Enhancing the performance of silicon photonics biosensors. PhD thesis, University of British
855 Columbia, 2017.
- 856 58. Yoshie, T.; Tang, L.; Su, S.Y. Optical microcavity: sensing down to single molecules and atoms. *Sensors* **2011**,
857 *11*, 1972–1991.
- 858 59. Blair, S.; Chen, Y. Resonant-enhanced evanescent-wave fluorescence biosensing with cylindrical optical cavities.
859 *Applied Optics* **2001**, *40*, 570–582.
- 860 60. Boyd, R.W.; Heebner, J.E. Sensitive disk resonator photonic biosensor. *Applied Optics* **2001**, *40*, 5742–5747.
- 861 61. Ksendzov, A.; Lin, Y. Integrated optics ring-resonator sensors for protein detection. *Optics letters* **2005**,
862 *30*, 3344–3346.
- 863 62. Krioukov, E.; Klunder, D.; Driessen, A.; Greve, J.; Otto, C. Sensor based on an integrated optical microcavity. *Optics
864 letters* **2002**, *27*, 512–514.

- 865 63. Armani, A.M.; Vahala, K.J. Heavy water detection using ultra-high-Q microcavities. *Optics Letters* **2006**,
866 31, 1896–1898.
- 867 64. Carlborg, C.F.; Gylfason, K.B.; Kaźmierczak, A.; Dortu, F.; Polo, M.B.; Catala, A.M.; Kresbach, G.M.; Sohlström, H.;
868 Moh, T.; Vivien, L.; others. A packaged optical slot-waveguide ring resonator sensor array for multiplex label-free
869 assays in labs-on-chips. *Lab on a Chip* **2010**, 10, 281–290.
- 870 65. Kazmierczak, A.; Dortu, F.; Schrevens, O.; Giannone, D.; Vivien, L.; Marris-Morini, D.; Bouville, D.; Cassan, E.;
871 Gylfason, K.B.; Sohlström, H.B.; others. Light coupling and distribution for Si₃N₄/SiO₂ integrated multichannel
872 single-mode sensing system. *Optical Engineering* **2009**, 48, 014401.
- 873 66. Yalcin, A.; Papat, K.C.; Aldridge, J.C.; Desai, T.A.; Hryniewicz, J.; Chbouki, N.; Little, B.E.; King, O.; Van, V.; Chu, S.;
874 others. Optical sensing of biomolecules using microring resonators. *IEEE Journal of Selected Topics in Quantum
875 Electronics* **2006**, 12, 148–155.
- 876 67. Ramachandran, A.; Wang, S.; Clarke, J.; Ja, S.; Goad, D.; Wald, L.; Flood, E.; Knobbe, E.; Hryniewicz, J.; Chu, S.;
877 others. A universal biosensing platform based on optical micro-ring resonators. *Biosensors and Bioelectronics*
878 **2008**, 23, 939–944.
- 879 68. Ciminelli, C.; Dell’Olio, F.; Conteduca, D.; Campanella, C.; Armenise, M. High performance SOI microring resonator
880 for biochemical sensing. *Optics & laser technology* **2014**, 59, 60–67.
- 881 69. Chao, C.Y.; Fung, W.; Guo, L.J. Polymer microring resonators for biochemical sensing applications. *IEEE journal of
882 selected topics in quantum electronics* **2006**, 12, 134–142.
- 883 70. Girault, P.; Lorrain, N.; Poffo, L.; Guendouz, M.; Lemaitre, J.; Carré, C.; Gadonna, M.; Bosc, D.; Vignaud, G. Integrated
884 polymer micro-ring resonators for optical sensing applications. *Journal of Applied Physics* **2015**, 117, 104504.
- 885 71. Iqbal, M.; Gleeson, M.A.; Spaug, B.; Tybor, E.; Gunn, W.G.; Hochberg, M.; Baehr-Jones, T.; Bailey, R.C.; Gunn, L.C.
886 Label-free biosensor arrays based on silicon ring resonators and high-speed optical scanning instrumentation.
887 *IEEE Journal of Selected Topics in Quantum Electronics* **2010**, 16, 654–661.
- 888 72. Chrostowski, L.; Hochberg, M. *Silicon photonics design: from devices to systems*; Cambridge University Press, 2015.
- 889 73. Hanumegowda, N.M.; Stica, C.J.; Patel, B.C.; White, I.; Fan, X. Refractometric sensors based on microsphere
890 resonators. *Applied Physics Letters* **2005**, 87, 201107.
- 891 74. Vollmer, E.; Arnold, S. Whispering-gallery-mode biosensing: label-free detection down to single molecules. *Nature
892 methods* **2008**, 5, 591.
- 893 75. Zhu, H.; White, I.M.; Suter, J.D.; Fan, X. Phage-based label-free biomolecule detection in an opto-fluidic ring
894 resonator. *Biosensors and Bioelectronics* **2008**, 24, 461–466.
- 895 76. Yang, G.; White, I.M.; Fan, X. An opto-fluidic ring resonator biosensor for the detection of organophosphorus
896 pesticides. *Sensors and Actuators B: Chemical* **2008**, 133, 105–112.
- 897 77. Gohring, J.T.; Dale, P.S.; Fan, X. Detection of HER2 breast cancer biomarker using the opto-fluidic ring resonator
898 biosensor. *Sensors and Actuators B: Chemical* **2010**, 146, 226–230.
- 899 78. Ren, H.C.; Vollmer, E.; Arnold, S.; Libchaber, A. High-Q microsphere biosensor-analysis for adsorption of rodlike
900 bacteria. *Optics Express* **2007**, 15, 17410–17423.
- 901 79. Hunt, H.K.; Soteropulos, C.; Armani, A.M. Bioconjugation strategies for microtoroidal optical resonators. *Sensors
902* **2010**, 10, 9317–9336.
- 903 80. Chow, E.; Grot, A.; Mirkarimi, L.; Sigalas, M.; Girolami, G. Ultracompact biochemical sensor built with
904 two-dimensional photonic crystal microcavity. *Optics letters* **2004**, 29, 1093–1095.
- 905 81. Rindorf, L.; Jensen, J.B.; Dufva, M.; Pedersen, L.H.; Høiby, P.E.; Bang, O. Photonic crystal fiber long-period gratings
906 for biochemical sensing. *Optics Express* **2006**, 14, 8224–8231.
- 907 82. Yang, D.; Tian, H.; Ji, Y. High-Q and high-sensitivity width-modulated photonic crystal single nanobeam air-mode
908 cavity for refractive index sensing. *Applied optics* **2015**, 54, 1–5.
- 909 83. Baker, J.E.; Sriram, R.; Miller, B.L. Two-dimensional photonic crystals for sensitive microscale chemical and
910 biochemical sensing. *Lab on a Chip* **2015**, 15, 971–990.
- 911 84. Yablonovitch, E. Inhibited spontaneous emission in solid-state physics and electronics. *Physical review letters*
912 **1987**, 58, 2059.
- 913 85. John, S. Strong localization of photons in certain disordered dielectric superlattices. *Physical review letters* **1987**,
914 58, 2486.
- 915 86. Lee, M.R.; Fauchet, P.M. Nanoscale microcavity sensor for single particle detection. *Optics letters* **2007**,
916 32, 3284–3286.

- 917 87. Cunningham, B.; Li, P.; Lin, B.; Pepper, J. Colorimetric resonant reflection as a direct biochemical assay technique.
918 *Sensors and Actuators B: Chemical* **2002**, *81*, 316–328.
- 919 88. Cunningham, B.; Qiu, J.; Li, P.; Lin, B. Enhancing the surface sensitivity of colorimetric resonant optical biosensors.
920 *Sensors and Actuators B: Chemical* **2002**, *87*, 365–370.
- 921 89. Cunningham, B.T.; Laing, L. Microplate-based, label-free detection of biomolecular interactions: applications in
922 proteomics. *Expert review of proteomics* **2006**, *3*, 271–281.
- 923 90. Chan, S.; Fauchet, P.; Li, Y.; Rothberg, L.; Miller, B. Porous silicon microcavities for biosensing applications. *physica*
924 *status solidi (a)* **2000**, *182*, 541–546.
- 925 91. Chan, S.; Horner, S.R.; Fauchet, P.M.; Miller, B.L. Identification of gram negative bacteria using nanoscale silicon
926 microcavities. *Journal of the American Chemical Society* **2001**, *123*, 11797–11798.
- 927 92. Ouyang, H.; Christophersen, M.; Viard, R.; Miller, B.L.; Fauchet, P.M. Macroporous silicon microcavities for
928 macromolecule detection. *Advanced Functional Materials* **2005**, *15*, 1851–1859.
- 929 93. García-Rupérez, J.; Toccafondo, V.; Bañuls, M.J.; Castelló, J.G.; Griol, A.; Peransi-Llopis, S.; Maquieira, Á. Label-free
930 antibody detection using band edge fringes in SOI planar photonic crystal waveguides in the slow-light regime.
931 *Optics Express* **2010**, *18*, 24276–24286.
- 932 94. Kang, C.; Weiss, S.M. Photonic crystal with multiple-hole defect for sensor applications. *Optics express* **2008**,
933 *16*, 18188–18193.
- 934 95. Kang, C.; Phare, C.T.; Vlasov, Y.A.; Assefa, S.; Weiss, S.M. Photonic crystal slab sensor with enhanced surface area.
935 *Optics express* **2010**, *18*, 27930–27937.
- 936 96. Qin, K.; Hu, S.; Retterer, S.T.; Kravchenko, I.I.; Weiss, S.M. Slow light Mach-Zehnder interferometer as label-free
937 biosensor with scalable sensitivity. *Optics letters* **2016**, *41*, 753–756.
- 938 97. Lo, S.M.; Hu, S.; Gaur, G.; Kostoulas, Y.; Weiss, S.M.; Fauchet, P.M. Photonic crystal microring resonator for
939 label-free biosensing. *Optics express* **2017**, *25*, 7046–7054.
- 940 98. Mandal, S.; Erickson, D. Nanoscale optofluidic sensor arrays. *Optics Express* **2008**, *16*, 1623–1631.
- 941 99. Pal, S.; Guillermain, E.; Sriram, R.; Miller, B.L.; Fauchet, P.M. Silicon photonic crystal nanocavity-coupled
942 waveguides for error-corrected optical biosensing. *Biosensors and Bioelectronics* **2011**, *26*, 4024–4031.
- 943 100. Zou, Y.; Chakravarty, S.; Zhu, L.; Chen, R.T. The role of group index engineering in series-connected photonic
944 crystal microcavities for high density sensor microarrays. *Applied physics letters* **2014**, *104*, 141103.
- 945 101. Zhou, J.; Huang, L.; Fu, Z.; Sun, F.; Tian, H. Multiplexed simultaneous high sensitivity sensors with high-order mode
946 based on the integration of photonic crystal 1 × 3 beam splitter and three different single-slot PCNCs. *Sensors*
947 **2016**, *16*, 1050.
- 948 102. Zhang, L.; Fu, Z.; Sun, F.; Wang, C.; Tian, H. Highly sensitive one chip eight channel sensing of ultra-compact
949 parallel integrated photonic crystal cavities based on silicon-on-insulator platform. Lasers and Electro-Optics
950 Pacific Rim (CLEO-PR), 2017 Conference on. IEEE, 2017, pp. 1–2.
- 951 103. Kersey, A.D.; Davis, M.A.; Patrick, H.J.; LeBlanc, M.; Koo, K.; Askins, C.; Putnam, M.; Friebele, E.J. Fiber grating
952 sensors. *Journal of lightwave technology* **1997**, *15*, 1442–1463.
- 953 104. Wang, X. Silicon photonic waveguide Bragg gratings. PhD thesis, University of British Columbia, 2013.
- 954 105. Schroeder, K.; Ecke, W.; Mueller, R.; Willsch, R.; Andreev, A. A fibre Bragg grating refractometer. *Measurement*
955 *Science and technology* **2001**, *12*, 757.
- 956 106. Lowder, T.L.; Gordon, J.D.; Schultz, S.M.; Selfridge, R.H. Volatile organic compound sensing using a surface-relief
957 D-shaped fiber Bragg grating and a polydimethylsiloxane layer. *Optics letters* **2007**, *32*, 2523–2525.
- 958 107. Guo, T.; Liu, F.; Liang, X.; Qiu, X.; Huang, Y.; Xie, C.; Xu, P.; Mao, W.; Guan, B.O.; Albert, J. Highly sensitive detection
959 of urinary protein variations using tilted fiber grating sensors with plasmonic nanocoatings. *Biosensors and*
960 *Bioelectronics* **2016**, *78*, 221–228.
- 961 108. Murphy, T.E.; Hastings, J.T.; Smith, H.I. Fabrication and characterization of narrow-band Bragg-reflection filters in
962 silicon-on-insulator ridge waveguides. *Journal of lightwave technology* **2001**, *19*, 1938.
- 963 109. Passaro, V.M.; Loiacono, R.; D'Amico, G.; De Leonardis, F. Design of Bragg grating sensors based on submicrometer
964 optical rib waveguides in SOI. *IEEE Sensors Journal* **2008**, *8*, 1603–1611.
- 965 110. Fard, S.T.; Grist, S.M.; Donzella, V.; Schmidt, S.A.; Flueckiger, J.; Wang, X.; Shi, W.; Millsbaugh, A.; Webb, M.;
966 Ratner, D.M.; others. Label-free silicon photonic biosensors for use in clinical diagnostics. Silicon Photonics VIII.
967 International Society for Optics and Photonics, 2013, Vol. 8629, p. 862909.
- 968 111. Luchansky, M.S.; Bailey, R.C. Silicon photonic microring resonators for quantitative cytokine detection and T-cell
969 secretion analysis. *Analytical chemistry* **2010**, *82*, 1975–1981.

- 970 112. McClellan, M.S.; Domier, L.L.; Bailey, R.C. Label-free virus detection using silicon photonic microring resonators.
971 *Biosensors and Bioelectronics* **2012**, *31*, 388–392.
- 972 113. Qavi, A.J.; Mysz, T.M.; Bailey, R.C. Isothermal discrimination of single-nucleotide polymorphisms via real-time
973 kinetic desorption and label-free detection of DNA using silicon photonic microring resonator arrays. *Analytical*
974 *chemistry* **2011**, *83*, 6827–6833.
- 975 114. Qavi, A.J.; Bailey, R.C. Multiplexed detection and label-free quantitation of MicroRNAs using arrays of silicon
976 photonic microring resonators. *Angewandte Chemie* **2010**, *122*, 4712–4715.
- 977 115. Luchansky, M.S.; Washburn, A.L.; McClellan, M.S.; Bailey, R.C. Sensitive on-chip detection of a protein biomarker
978 in human serum and plasma over an extended dynamic range using silicon photonic microring resonators and
979 sub-micron beads. *Lab on a Chip* **2011**, *11*, 2042–2044.
- 980 116. Sepúlveda, B.; Armelles, G.; Lechuga, L. Magneto-optical phase modulation in integrated Mach-Zehnder
981 interferometric sensors. *Sensors and Actuators A: Physical* **2007**, *134*, 339–347.
- 982 117. Densmore, A.; Xu, D.X.; Janz, S.; Waldron, P.; Lapointe, J.; Mischki, T.; Lopinski, G.; Delâge, A.; Schmid, J.; Cheben, P.
983 Sensitive label-free biomolecular detection using thin silicon waveguides. *Advances in optical technologies* **2008**,
984 *2008*.
- 985 118. Xu, D.X.; Vachon, M.; Densmore, A.; Ma, R.; Janz, S.; Delâge, A.; Lapointe, J.; Cheben, P.; Schmid, J.; Post, E.; others.
986 Real-time cancellation of temperature induced resonance shifts in SOI wire waveguide ring resonator label-free
987 biosensor arrays. *Optics Express* **2010**, *18*, 22867–22879.
- 988 119. Barrios, C.A. Optical slot-waveguide based biochemical sensors. *Sensors* **2009**, *9*, 4751–4765.
- 989 120. Baehr-Jones, T.; Hochberg, M.; Walker, C.; Scherer, A. High-Q optical resonators in silicon-on-insulator-based slot
990 waveguides. *Applied Physics Letters* **2005**, *86*, 081101.
- 991 121. Barrios, C.A.; Gylfason, K.B.; Sánchez, B.; Griol, A.; Sohlström, H.; Holgado, M.; Casquel, R. Slot-waveguide
992 biochemical sensor. *Optics letters* **2007**, *32*, 3080–3082.
- 993 122. Claes, T.; Molera, J.G.; De Vos, K.; Schacht, E.; Baets, R.; Bienstman, P. Label-free biosensing with a
994 slot-waveguide-based ring resonator in silicon on insulator. *IEEE Photonics journal* **2009**, *1*, 197–204.
- 995 123. Taniguchi, T.; Hirowatari, A.; Ikeda, T.; Fukuyama, M.; Amemiya, Y.; Kuroda, A.; Yokoyama, S. Detection of
996 antibody-antigen reaction by silicon nitride slot-ring biosensors using protein G. *Optics Communications* **2016**,
997 *365*, 16–23.
- 998 124. Zhang, W.; Serna, S.; Le Roux, X.; Vivien, L.; Cassan, E. Highly sensitive refractive index sensing by fast detuning
999 the critical coupling condition of slot waveguide ring resonators. *Optics letters* **2016**, *41*, 532–535.
- 1000 125. Barrios, C.A. Ultrasensitive nanomechanical photonic sensor based on horizontal slot-waveguide resonator. *IEEE*
1001 *Photonics Technology Letters* **2006**, *18*, 2419–2421.
- 1002 126. Lee, S.; Eom, S.C.; Chang, J.S.; Huh, C.; Sung, G.Y.; Shin, J.H. Label-free optical biosensing using a horizontal
1003 air-slot SiN_x microdisk resonator. *Optics express* **2010**, *18*, 20638–20644.
- 1004 127. Kim, G.; Shin, J.H. Luminescent silicon-rich nitride horizontal air-slot microdisk resonators for biosensing. *IEEE*
1005 *Photonics Technology Letters* **2016**, *28*, 2331–2334.
- 1006 128. Tu, X.; Song, J.; Liow, T.Y.; Park, M.K.; Yiying, J.Q.; Kee, J.S.; Yu, M.; Lo, G.Q. Thermal independent silicon-nitride
1007 slot waveguide biosensor with high sensitivity. *Optics express* **2012**, *20*, 2640–2648.
- 1008 129. Wang, X.; Flueckiger, J.; Schmidt, S.; Grist, S.; Fard, S.T.; Kirk, J.; Doerfler, M.; Cheung, K.C.; Ratner, D.M.;
1009 Chrostowski, L. A silicon photonic biosensor using phase-shifted Bragg gratings in slot waveguide. *Journal of*
1010 *biophotonics* **2013**, *6*, 821–828.
- 1011 130. Lai, W.C.; Chakravarty, S.; Wang, X.; Lin, C.; Chen, R.T. On-chip methane sensing by near-IR absorption signatures
1012 in a photonic crystal slot waveguide. *Optics letters* **2011**, *36*, 984–986.
- 1013 131. Scullion, M.G.; Krauss, T.F.; Di Falco, A. Slotted photonic crystal sensors. *Sensors* **2013**, *13*, 3675–3710.
- 1014 132. Di Falco, A.; O'faolain, L.; Krauss, T. Chemical sensing in slotted photonic crystal heterostructure cavities. *Applied*
1015 *physics letters* **2009**, *94*, 063503.
- 1016 133. Jágerská, J.; Zhang, H.; Diao, Z.; Le Thomas, N.; Houdré, R. Refractive index sensing with an air-slot photonic
1017 crystal nanocavity. *Optics letters* **2010**, *35*, 2523–2525.
- 1018 134. Liu, Q.; Tu, X.; Kim, K.W.; Kee, J.S.; Shin, Y.; Han, K.; Yoon, Y.J.; Lo, G.Q.; Park, M.K. Highly sensitive Mach-Zehnder
1019 interferometer biosensor based on silicon nitride slot waveguide. *Sensors and Actuators B: Chemical* **2013**,
1020 *188*, 681–688.
- 1021 135. Sun, X.; Dai, D.; Thylén, L.; Wosinski, L. High-sensitivity liquid refractive-index sensor based on a Mach-Zehnder
1022 interferometer with a double-slot hybrid plasmonic waveguide. *Optics express* **2015**, *23*, 25688–25699.

- 1023 136. Fard, S.T.; Donzella, V.; Schmidt, S.A.; Flueckiger, J.; Grist, S.M.; Fard, P.T.; Wu, Y.; Bojko, R.J.; Kwok, E.; Jaeger,
1024 N.A.; others. Performance of ultra-thin SOI-based resonators for sensing applications. *Optics express* **2014**,
1025 22, 14166–14179.
- 1026 137. Veldhuis, G.; Parriaux, O.; Hoekstra, H.; Lambeck, P. Sensitivity enhancement in evanescent optical waveguide
1027 sensors. *Journal of lightwave technology* **2000**, 18, 677.
- 1028 138. Wang, X.; Guan, X.; Huang, Q.; Zheng, J.; Shi, Y.; Dai, D. Suspended ultra-small disk resonator on silicon for optical
1029 sensing. *Optics letters* **2013**, 38, 5405–5408.
- 1030 139. Hu, S.; Qin, K.; Kravchenko, I.I.; Retterer, S.T.; Weiss, S.M. Suspended micro-ring resonator for enhanced
1031 biomolecule detection sensitivity. *Frontiers in Biological Detection: From Nanosensors to Systems VI*. International
1032 Society for Optics and Photonics, 2014, Vol. 8933, p. 893306.
- 1033 140. Taha, A.M.; Paredes, B.; Khilo, A.; Dahlem, M.S. SOI-based centimeter-scale Mach-Zehnder interferometers for
1034 fluid sensing. *Integrated Optics: Devices, Materials, and Technologies XXI*. International Society for Optics and
1035 Photonics, 2017, Vol. 10106, p. 101060N.
- 1036 141. Kou, L.; Labrie, D.; Chylek, P. Refractive indices of water and ice in the 0.65- to 2.5- μm spectral range. *Applied*
1037 *optics* **1993**, 32, 3531–3540.
- 1038 142. Melnik, E.; Bruck, R.; Müellner, P.; Schleder, T.; Hainberger, R.; Lämmerhofer, M. Human IgG detection in serum
1039 on polymer based Mach-Zehnder interferometric biosensors. *Journal of biophotonics* **2016**, 9, 218–223.
- 1040 143. Kim, J.H.E.; Chrostowski, L.; Bisailon, E.; Plant, D.V. DBR, Sub-wavelength grating, and Photonic crystal slab
1041 Fabry-Perot cavity design using phase analysis by FDTD. *Optics express* **2007**, 15, 10330–10339.
- 1042 144. Cheben, P.; Xu, D.X.; Janz, S.; Densmore, A. Subwavelength waveguide grating for mode conversion and light
1043 coupling in integrated optics. *Optics express* **2006**, 14, 4695–4702.
- 1044 145. Bock, P.J.; Cheben, P.; Schmid, J.H.; Lapointe, J.; Delâge, A.; Janz, S.; Aers, G.C.; Xu, D.X.; Densmore, A.; Hall, T.J.
1045 Subwavelength grating periodic structures in silicon-on-insulator: a new type of microphotonic waveguide. *Optics*
1046 *express* **2010**, 18, 20251–20262.
- 1047 146. Cheben, P.; Bock, P.J.; Schmid, J.H.; Lapointe, J.; Janz, S.; Xu, D.X.; Densmore, A.; Delâge, A.; Lamontagne, B.; Hall,
1048 T.J. Refractive index engineering with subwavelength gratings for efficient microphotonic couplers and planar
1049 waveguide multiplexers. *Optics letters* **2010**, 35, 2526–2528.
- 1050 147. Halir, R.; Bock, P.J.; Cheben, P.; Ortega-Moñux, A.; Alonso-Ramos, C.; Schmid, J.H.; Lapointe, J.; Xu, D.X.;
1051 Wangüemert-Pérez, J.G.; Molina-Fernández, Í.; others. Waveguide sub-wavelength structures: a review of
1052 principles and applications. *Laser & Photonics Reviews* **2015**, 9, 25–49.
- 1053 148. Cheben, P.; Halir, R.; Schmid, J.H.; Atwater, H.A.; Smith, D.R. Subwavelength integrated photonics. *Nature* **2018**,
1054 560, 565.
- 1055 149. Weissman, Z.; Hendel, I. Analysis of periodically segmented waveguide mode expanders. *Journal of lightwave*
1056 *technology* **1995**, 13, 2053–2058.
- 1057 150. Wangüemert-Pérez, J.G.; Cheben, P.; Ortega-Moñux, A.; Alonso-Ramos, C.; Pérez-Galacho, D.; Halir, R.;
1058 Molina-Fernández, I.; Xu, D.X.; Schmid, J.H. Evanescent field waveguide sensing with subwavelength grating
1059 structures in silicon-on-insulator. *Optics letters* **2014**, 39, 4442–4445.
- 1060 151. Wang, Z.; Xu, X.; Fan, D.; Wang, Y.; Chen, R.T. High quality factor subwavelength grating waveguide micro-ring
1061 resonator based on trapezoidal silicon pillars. *Optics letters* **2016**, 41, 3375–3378.
- 1062 152. Yan, H.; Huang, L.; Xu, X.; Chakravarty, S.; Tang, N.; Tian, H.; Chen, R.T. Unique surface sensing property and
1063 enhanced sensitivity in microring resonator biosensors based on subwavelength grating waveguides. *Optics*
1064 *express* **2016**, 24, 29724–29733.
- 1065 153. Huang, L.; Yan, H.; Xu, X.; Chakravarty, S.; Tang, N.; Tian, H.; Chen, R.T. Improving the detection limit for on-chip
1066 photonic sensors based on subwavelength grating racetrack resonators. *Optics express* **2017**, 25, 10527–10535.
- 1067 154. Donzella, V.; Sherwali, A.; Flueckiger, J.; Grist, S.M.; Fard, S.T.; Chrostowski, L. Design and fabrication of SOI
1068 micro-ring resonators based on sub-wavelength grating waveguides. *Optics express* **2015**, 23, 4791–4803.
- 1069 155. Flueckiger, J.; Schmidt, S.; Donzella, V.; Sherwali, A.; Ratner, D.M.; Chrostowski, L.; Cheung, K.C. Sub-wavelength
1070 grating for enhanced ring resonator biosensor. *Optics express* **2016**, 24, 15672–15686.
- 1071 156. Luan, E.; Yun, H.; Laplatine, L.; Dattner, Y.; Ratner, D.M.; Cheung, K.; Chrostowski, L. Enhanced sensitivity of
1072 sub-wavelength multi-box waveguide microring resonator label-free biosensor. *IEEE Journal of Selected Topics in*
1073 *Quantum Electronics* **2018**.

- 1074 157. Luan, E.; Yun, H.; Laplatine, L.; Flückiger, J.; Dattner, Y.; Ratner, D.; Cheung, K.; Chrostowski, L. Sub-wavelength
1075 multi-box waveguide-based label-free sensors. *Integrated Optics: Devices, Materials, and Technologies XXII*.
1076 International Society for Optics and Photonics, 2018, Vol. 10535, p. 105350H.
- 1077 158. Sumi, R.; Gupta, N.D.; Das, B.K. Integrated optical Mach-Zehnder interferometer with a sensing arm of
1078 sub-wavelength grating waveguide in SOI. *SENSORS*, 2017 IEEE. IEEE, 2017, pp. 1–3.
- 1079 159. Dai, D. Highly sensitive digital optical sensor based on cascaded high-Q ring-resonators. *Optics Express* **2009**,
1080 *17*, 23817–23822.
- 1081 160. Claes, T.; Bogaerts, W.; Bienstman, P. Experimental characterization of a silicon photonic biosensor consisting
1082 of two cascaded ring resonators based on the Vernier-effect and introduction of a curve fitting method for an
1083 improved detection limit. *Optics express* **2010**, *18*, 22747–22761.
- 1084 161. Jiang, X.; Chen, Y.; Yu, F.; Tang, L.; Li, M.; He, J.J. High-sensitivity optical biosensor based on cascaded
1085 Mach-Zehnder interferometer and ring resonator using Vernier effect. *Optics letters* **2014**, *39*, 6363–6366.
- 1086 162. Liu, B.; Shakouri, A.; Bowers, J.E. Wide tunable double ring resonator coupled lasers. *IEEE Photonics Technology*
1087 *Letters* **2002**, *14*, 600–602.
- 1088 163. Madsen, C.K.; Zhao, J.H. *Optical filter design and analysis*; Wiley New York, 1999.
- 1089 164. Rabiei, P.; Steier, W.H. Tunable polymer double micro-ring filters. *IEEE Photonics Technology Letters* **2003**,
1090 *15*, 1255–1257.
- 1091 165. Jin, L.; Li, M.; He, J.J. Highly-sensitive silicon-on-insulator sensor based on two cascaded micro-ring resonators
1092 with vernier effect. *Optics Communications* **2011**, *284*, 156–159.
- 1093 166. Jiang, X.; Ye, J.; Zou, J.; Li, M.; He, J.J. Cascaded silicon-on-insulator double-ring sensors operating in
1094 high-sensitivity transverse-magnetic mode. *Optics letters* **2013**, *38*, 1349–1351.
- 1095 167. Hu, J.; Dai, D. Cascaded-ring optical sensor with enhanced sensitivity by using suspended Si-nanowires. *IEEE*
1096 *Photonics Technology Letters* **2011**, *23*, 842–844.
- 1097 168. Passaro, V.M.; Troia, B.; De Leonardis, F. A generalized approach for design of photonic gas sensors based on
1098 Vernier-effect in mid-IR. *Sensors and Actuators B: Chemical* **2012**, *168*, 402–420.
- 1099 169. Liu, Y.; Li, Y.; Li, M.; He, J.J. High-sensitivity and wide-range optical sensor based on three cascaded ring resonators.
1100 *Optics Express* **2017**, *25*, 972–978.
- 1101 170. La Notte, M.; Passaro, V.M. Ultra high sensitivity chemical photonic sensing by Mach-Zehnder interferometer
1102 enhanced Vernier-effect. *Sensors and Actuators B: Chemical* **2013**, *176*, 994–1007.
- 1103 171. Huang, L.; Tian, H.; Zhou, J.; Liu, Q.; Zhang, P.; Ji, Y. Label-free optical sensor by designing a high-Q photonic
1104 crystal ring-slot structure. *Optics Communications* **2015**, *335*, 73–77.
- 1105 172. Li, T.; Gao, D.; Zhang, D.; Cassan, E. High-Q and high-sensitivity one-dimensional photonic crystal slot nanobeam
1106 cavity sensors. *IEEE Photonics Technol. Lett.* **2016**, *28*, 689–692.
- 1107 173. Syahir, A.; Usui, K.; Tomizaki, K.y.; Kajikawa, K.; Mihara, H. Label and label-free detection techniques for protein
1108 microarrays. *Microarrays* **2015**, *4*, 228–244.
- 1109 174. Vestergaard, M.; Kerman, K.; Tamiya, E.; others. An overview of label-free electrochemical protein sensors. *Sensors*
1110 **2007**, *7*, 3442–3458.
- 1111 175. Stern, E.; Klemic, J.F.; Routenberg, D.A.; Wyrembak, P.N.; Turner-Evans, D.B.; Hamilton, A.D.; LaVan, D.A.; Fahmy,
1112 T.M.; Reed, M.A. Label-free immunodetection with CMOS-compatible semiconducting nanowires. *Nature* **2007**,
1113 *445*, 519.
- 1114 176. Hunt, H.K.; Armani, A.M. Label-free biological and chemical sensors. *Nanoscale* **2010**, *2*, 1544–1559.
- 1115 177. Cunningham, B.T.; Laing, L.G. Advantages and application of label-free detection assays in drug screening. *Expert*
1116 *opinion on drug discovery* **2008**, *3*, 891–901.
- 1117 178. Xu, J.; Suarez, D.; Gottfried, D.S. Detection of avian influenza virus using an interferometric biosensor. *Analytical*
1118 *and bioanalytical chemistry* **2007**, *389*, 1193–1199.
- 1119 179. Ymeti, A.; Greve, J.; Lambeck, P.V.; Wink, T.; van Hövell, S.W.; Beumer, T.A.; Wijn, R.R.; Heideman, R.G.;
1120 Subramaniam, V.; Kanger, J.S. Fast, ultrasensitive virus detection using a Young interferometer sensor. *Nano letters*
1121 **2007**, *7*, 394–397.
- 1122 180. Pal, S.; Yadav, A.R.; Lifson, M.A.; Baker, J.E.; Fauchet, P.M.; Miller, B.L. Selective virus detection in complex sample
1123 matrices with photonic crystal optical cavities. *Biosensors and Bioelectronics* **2013**, *44*, 229–234.
- 1124 181. Chen, Y.; Yu, F.; Yang, C.; Song, J.; Tang, L.; Li, M.; He, J.J. Label-free biosensing using cascaded double-microring
1125 resonators integrated with microfluidic channels. *Optics Communications* **2015**, *344*, 129–133.

- 1126 182. Weisser, M.; Tovar, G.; Mittler-Neher, S.; Knoll, W.; Brosinger, F.; Freimuth, H.; Lacher, M.; Ehrfeld, W. Specific
1127 bio-recognition reactions observed with an integrated Mach-Zehnder interferometer. *Biosensors and Bioelectronics*
1128 **1999**, *14*, 405–411.
- 1129 183. Buswell, S.; Wright, V.; Buriak, J.; Van, V.; Evoy, S. Specific detection of proteins using photonic crystal waveguides.
1130 *Optics Express* **2008**, *16*, 15949–15957.
- 1131 184. Zou, Y.; Chakravarty, S.; Kwong, D.N.; Lai, W.C.; Xu, X.; Lin, X.; Hosseini, A.; Chen, R.T. Cavity-waveguide coupling
1132 engineered high sensitivity silicon photonic crystal microcavity biosensors with high yield. *IEEE Journal of Selected*
1133 *Topics in Quantum Electronics* **2014**, *20*, 171–180.
- 1134 185. Martincek, I.; Kacik, D. A PDMS microfiber Mach-Zehnder interferometer and determination of nanometer
1135 displacements. *Optical Fiber Technology* **2018**, *40*, 13–17.
- 1136 186. Ymeti, A.; Kanger, J.S.; Greve, J.; Besselink, G.; Lambeck, P.; Wijn, R.; Heideman, R. Integration of microfluidics
1137 with a four-channel integrated optical Young interferometer immunosensor. *Biosensors and Bioelectronics* **2005**,
1138 *20*, 1417–1421.
- 1139 187. De Vos, K.; Girones, J.; Claes, T.; De Koninck, Y.; Popelka, S.; Schacht, E.; Baets, R.; Bienstman, P. Multiplexed
1140 antibody detection with an array of silicon-on-insulator microring resonators. *IEEE Photonics Journal* **2009**,
1141 *1*, 225–235.
- 1142 188. Washburn, A.L.; Luchansky, M.S.; Bowman, A.L.; Bailey, R.C. Quantitative, label-free detection of five protein
1143 biomarkers using multiplexed arrays of silicon photonic microring resonators. *Analytical chemistry* **2009**, *82*, 69–72.
- 1144 189. Psarouli, A.; Botsialas, A.; Salapatias, A.; Stefanitsis, G.; Nikita, D.; Jobst, G.; Chaniotakis, N.; Goustouridis, D.;
1145 Makarona, E.; Petrou, P.S.; others. Fast label-free detection of C-reactive protein using broad-band Mach-Zehnder
1146 interferometers integrated on silicon chips. *Talanta* **2017**, *165*, 458–465.
- 1147 190. Martens, D.; Priego, P.R.; Murib, M.S.; Elamin, A.; Gonzalez-Guerrero, A.B.; Stehr, M.; Jonas, E.; Anton, B.; Hlawatsch,
1148 N.; Soetaert, P.; others. Low-cost integrated biosensing platform based on SiN nanophotonics for biomarker
1149 detection in urine. *Analytical Methods* **2018**.
- 1150 191. Scheler, O.; Kindt, J.T.; Qavi, A.J.; Kaplinski, L.; Glynn, B.; Barry, T.; Kurg, A.; Bailey, R.C. Label-free, multiplexed
1151 detection of bacterial tmRNA using silicon photonic microring resonators. *Biosensors and Bioelectronics* **2012**,
1152 *36*, 56–61.
- 1153 192. Qavi, A.J.; Bailey, R.C. Multiplexed Detection and Label-Free Quantitation of MicroRNAs Using Arrays of Silicon
1154 Photonic Microring Resonators. *Angewandte Chemie International Edition* **2010**, *49*, 4608–4611.
- 1155 193. Liu, Q.; Shin, Y.; Kee, J.S.; Kim, K.W.; Rafei, S.R.M.; Perera, A.P.; Tu, X.; Lo, G.Q.; Ricci, E.; Colombel, M.; others.
1156 Mach-Zehnder interferometer (MZI) point-of-care system for rapid multiplexed detection of microRNAs in human
1157 urine specimens. *Biosensors and Bioelectronics* **2015**, *71*, 365–372.
- 1158 194. Sepúlveda, B.; Del Rio, J.S.; Moreno, M.; Blanco, F.; Mayora, K.; Domínguez, C.; Lechuga, L. Optical biosensor
1159 microsystems based on the integration of highly sensitive Mach-Zehnder interferometer devices. *Journal of Optics*
1160 *A: Pure and Applied Optics* **2006**, *8*, S561.
- 1161 195. Toccafondo, V.; García-Rupérez, J.; Bañuls, M.; Griol, A.; Castelló, J.; Peransi-Llopis, S.; Maquieira, A. Single-strand
1162 DNA detection using a planar photonic-crystal-waveguide-based sensor. *Optics letters* **2010**, *35*, 3673–3675.
- 1163 196. Yan, H.; Yang, C.J.; Tang, N.; Zou, Y.; Chakravarty, S.; Roth, A.; Chen, R.T. Specific Detection of Antibiotics by
1164 Silicon-on-Chip Photonic Crystal Biosensor Arrays. *IEEE Sensors Journal* **2017**, *17*, 5915–5919.
- 1165 197. Romano, S.; Zito, G.; Torino, S.; Calafiore, G.; Penzo, E.; Coppola, G.; Cabrini, S.; Rendina, I.; Mocella, V. Label-free
1166 sensing of ultralow-weight molecules with all-dielectric metasurfaces supporting bound states in the continuum.
1167 *Photonics Research* **2018**, *6*, 726–733.
- 1168 198. Schumacher, S.; Nestler, J.; Otto, T.; Wegener, M.; Ehrentreich-Förster, E.; Michel, D.; Wunderlich, K.; Palzer, S.;
1169 Sohn, K.; Weber, A.; others. Highly-integrated lab-on-chip system for point-of-care multiparameter analysis. *Lab*
1170 *on a Chip* **2012**, *12*, 464–473.
- 1171 199. Xu, D.X.; Schmid, J.H.; Reed, G.T.; Mashanovich, G.Z.; Thomson, D.J.; Nedeljkovic, M.; Chen, X.; Van Thourhout, D.;
1172 Keyvaninia, S.; Selvaraja, S.K. Silicon photonic integration platform—Have we found the sweet spot? *IEEE Journal*
1173 *of Selected Topics in Quantum Electronics* **2014**, *20*, 189–205.
- 1174 200. Liu, K.K.; Wu, R.G.; Chuang, Y.J.; Khoo, H.S.; Huang, S.H.; Tseng, F.G. Microfluidic systems for biosensing. *Sensors*
1175 **2010**, *10*, 6623–6661.
- 1176 201. Wang, Z.; Yan, H.; Chakravarty, S.; Subbaraman, H.; Xu, X.; Fan, D.; Wang, A.X.; Chen, R.T. Microfluidic
1177 channels with ultralow-loss waveguide crossings for various chip-integrated photonic sensors. *Optics letters* **2015**,
1178 *40*, 1563–1566.

- 1179 202. Fan, X.; White, I.M. Optofluidic microsystems for chemical and biological analysis. *Nature photonics* **2011**, *5*, 591.
- 1180 203. Temiz, Y.; Lovchik, R.D.; Kaigala, G.V.; Delamarche, E. Lab-on-a-chip devices: How to close and plug the lab?
1181 *Microelectronic Engineering* **2015**, *132*, 156–175.
- 1182 204. Bhattacharya, S.; Datta, A.; Berg, J.M.; Gangopadhyay, S. Studies on surface wettability of poly(dimethyl)siloxane
1183 (PDMS) and glass under oxygen-plasma treatment and correlation with bond strength. *Journal of*
1184 *microelectromechanical systems* **2005**, *14*, 590–597.
- 1185 205. Temiz, Y.; Lovchik, R.D.; Kaigala, G.V.; Delamarche, E. Lab-on-a-chip devices: How to close and plug the lab?
1186 *Microelectronic Engineering* **2015**, *132*, 156–175.
- 1187 206. Laplatine, L.; Al'Mrayat, O.; Luan, E.; Fang, C.; Rezaiezhadeh, S.; Ratner, D.; Cheung, K.; Dattner, Y.; Chrostowski, L.
1188 System-level integration of active silicon photonic biosensors. Microfluidics, BioMEMS, and Medical Microsystems
1189 XV. International Society for Optics and Photonics, 2017, Vol. 10061, p. 100610I.
- 1190 207. Kamande, J.; Wang, Y.; Taylor, A. Cloning SU8 silicon masters using epoxy resins to increase feature replicability
1191 and production for cell culture devices. *Biomicrofluidics* **2015**, *9*, 036502.
- 1192 208. Lipka, T.; Moldenhauer, L.; Wahn, L.; Trieu, H. Optofluidic biomolecule sensors based on a-Si: H microrings
1193 embedded in silicon-glass microchannels. *Optics letters* **2017**, *42*, 1084–1087.
- 1194 209. Geidel, S.; Peransi Llopis, S.; Rodrigo, M.; de Diego-Castilla, G.; Sousa, A.; Nestler, J.; Otto, T.; Gessner, T.; Parro,
1195 V. Integration of an optical ring resonator biosensor into a self-contained microfluidic cartridge with active,
1196 single-shot micropumps. *Micromachines* **2016**, *7*, 153.
- 1197 210. Augel, L.; Berkmann, F.; Latta, D.; Fischer, I.; Bechler, S.; Elogail, Y.; KostECKI, K.; Potje-Kamloth, K.; Schulze,
1198 J. Optofluidic sensor system with Ge PIN photodetector for CMOS-compatible sensing. *Microfluidics and*
1199 *Nanofluidics* **2017**, *21*, 169.
- 1200 211. Hartley, L.; Kaler, K.V.; Yadid-Pecht, O. Hybrid integration of an active pixel sensor and microfluidics for cytometry
1201 on a chip. *IEEE Transactions on Circuits and Systems I: Regular Papers* **2007**, *54*, 99–110.
- 1202 212. Arce, C.L.; Witters, D.; Puers, R.; Lammertyn, J.; Bienstman, P. Silicon photonic sensors incorporated in a digital
1203 microfluidic system. *Analytical and bioanalytical chemistry* **2012**, *404*, 2887–2894.
- 1204 213. Luan, L.; Evans, R.D.; Jokerst, N.M.; Fair, R.B. Integrated optical sensor in a digital microfluidic platform. *IEEE*
1205 *Sensors Journal* **2008**, *8*, 628–635.
- 1206 214. Luan, L.; Royal, M.W.; Evans, R.; Fair, R.B.; Jokerst, N.M. Chip scale optical microresonator sensors integrated with
1207 embedded thin film photodetectors on electrowetting digital microfluidics platforms. *IEEE Sensors Journal* **2012**,
1208 *12*, 1794–1800.
- 1209 215. Luan, L.; Evans, R.; Schwinn, D.; Fair, R.; Jokerst, N. Chip scale integration of optical microresonator sensors with
1210 digital microfluidics systems. Lasers and Electro-Optics Society, 2008. LEOS 2008. 21st Annual Meeting of the IEEE.
1211 IEEE, 2008, pp. 259–260.
- 1212 216. Nestler, J.; Morschhauser, A.; Hiller, K.; Otto, T.; Bigot, S.; Auerswald, J.; Knapp, H.; Gavillet, J.; Gessner, T. Polymer
1213 lab-on-chip systems with integrated electrochemical pumps suitable for large-scale fabrication. *The International*
1214 *Journal of Advanced Manufacturing Technology* **2010**, *47*, 137–145.
- 1215 217. Liang, D.; Bowers, J.E. Recent progress in lasers on silicon. *Nat. Photonics* **2010**, *4*, 511–517.
- 1216 218. Zhou, Z.; Yin, B.; Michel, J. On-chip light sources for silicon photonics. *Light: Science & Applications* **2015**,
1217 *4*, e358–e358.
- 1218 219. Pavesi, L.; Dal Negro, L.; Mazzoleni, C.; Franzò, G.; Priolo, F. Optical gain in silicon nanocrystals. *Nature* **2000**,
1219 *408*, 440–444.
- 1220 220. Rong, H.; Liu, A.; Jones, R.; Cohen, O.; Hak, D.; Nicolaescu, R.; Fang, A.; Paniccia, M. An all-silicon Raman laser.
1221 *Nature* **2005**, *433*, 292–294.
- 1222 221. Camacho-Aguilera, R.E.; Cai, Y.; Patel, N.; Bessette, J.T.; Romagnoli, M.; Kimerling, L.C.; Michel, J. An electrically
1223 pumped germanium laser. *Opt. Express* **2012**, *20*, 11316.
- 1224 222. Liu, J.; Sun, X.; Pan, D.; Wang, X.; Kimerling, L.C.; Koch, T.L.; Michel, J. Tensile-strained, n-type Ge as a gain
1225 medium for monolithic laser integration on Si. *Opt. Express* **2007**, *15*, 11272.
- 1226 223. Kato, K.; Tohmori, Y. PLC hybrid integration technology and its application to photonic components. *IEEE J. Sel.*
1227 *Top. Quantum Electron.* **2000**, *6*, 4–13.
- 1228 224. Friedrich, E.E.L.; Oberg, M.G.; Broberg, B.; Nilsson, S.; Valette, S. Hybrid integration of semiconductor lasers with
1229 Si-based single-mode ridge waveguides. *J. Lightwave Technol.* **1992**, *10*, 336–340.

- 1230 225. Sasaki, J.; Itoh, M.; Tamanuki, T.; Hatakeyama, H.; Kitamura, S.; Shimoda, T.; Kato, T. Multiple-chip precise
1231 self-aligned assembly for hybrid integrated optical modules using Au-Sn solder bumps. *IEEE Trans. Adv. Packag.*
1232 **2001**, *24*, 569–575.
- 1233 226. Seassal, C.; Rojo-Romeo, P.; Letartre, X.; Viktorovitch, P.; Hollinger, G.; Jalaguier, E.; Pocas, S.; Aspar, B. InP microdisk
1234 lasers on silicon wafer: CW room temperature operation at 1.6 μm . *Electron. Lett.* **2001**, *37*, 222.
- 1235 227. Hattori, H.T.; Seassal, C.; Touraille, E.; Rojo-Romeo, P.; Letartre, X.; Hollinger, G.; Viktorovitch, P.; Di Cioccio, L.;
1236 Zussy, M.; Melhaoui, L.E.; Fedeli, J.M. Heterogeneous integration of microdisk lasers on silicon strip waveguides
1237 for optical interconnects. *IEEE Photonics Technol. Lett.* **2006**, *18*, 223–225.
- 1238 228. Mino, S.; Yoshino, K.; Yamada, Y.; Terui, T.; Yasu, M.; Moriwaki, K. Planar lightwave circuit platform with coplanar
1239 waveguide for opto-electronic hybrid integration. *J. Lightwave Technol.* **1995**, *13*, 2320–2326.
- 1240 229. Urino, Y.; Usuki, T.; Fujikata, J.; Ishizaka, M.; Yamada, K.; Horikawa, T.; Nakamura, T.; Arakawa, Y. High-density
1241 optical interconnects by using silicon photonics. Next-Generation Optical Networks for Data Centers and
1242 Short-Reach Links, 2014.
- 1243 230. Santis, C.T.; Steger, S.T.; Vilenchik, Y.; Vasilyev, A.; Yariv, A. High-coherence semiconductor lasers based on
1244 integral high-Q resonators in hybrid Si/III-V platforms. *Proceedings of the National Academy of Sciences* **2014**,
1245 *111*, 2879–2884.
- 1246 231. Roelkens, G.; Abassi, A.; Cardile, P.; Dave, U.; De Groote, A.; De Koninck, Y.; Dhoore, S.; Fu, X.; Gassenq, A.; Hattasan,
1247 N.; others. III-V-on-silicon photonic devices for optical communication and sensing. Photonics. Multidisciplinary
1248 Digital Publishing Institute, 2015, Vol. 2, pp. 969–1004.
- 1249 232. Lee, J.H.; Lee, D.Y.; Shubin, I.; Bovington, J.; Djordjevic, S.S.; Lin, S.; Luo, Y.; Yao, J.; Cunningham, J.E.; Raj, K.; others.
1250 III-V/Si hybrid laser stabilization using micro-ring feedback control. *IEEE Photonics J.* **2016**, *8*, 1–7.
- 1251 233. Lin, S.; Zheng, X.; Yao, J.; Djordjevic, S.S.; Cunningham, J.E.; Lee, J.H.; Shubin, I.; Luo, Y.; Bovington, J.; Lee, D.Y.;
1252 others. Efficient, tunable flip-chip-integrated III-V/Si hybrid external-cavity laser array. *Optics express* **2016**,
1253 *24*, 21454–21462.
- 1254 234. Ohtsubo, J. Feedback Induced Instability and Chaos in Semiconductor Lasers and Their Applications. *Opt. Rev.*
1255 **1999**, *6*, 1–15.
- 1256 235. Roelkens, G. III-V-on-silicon photonic integrated circuits for optical communication and sensing. *Frontiers in*
1257 *Optics* 2016, 2016.
- 1258 236. Park, H.; Fang, A.W.; Kodama, S.; Bowers, J.E. Hybrid silicon evanescent laser fabricated with a silicon waveguide
1259 and III-V offset quantum wells. *Opt. Express* **2005**, *13*, 9460.
- 1260 237. Fang, A.W.; Park, H.; Cohen, O.; Jones, R.; Paniccia, M.J.; Bowers, J.E. Electrically pumped hybrid AlGaInAs-silicon
1261 evanescent laser. *Opt. Express* **2006**, *14*, 9203.
- 1262 238. Welcome Aurion to Juniper Networks. [https://forums.juniper.net/t5/Engineering-Simplicity/Welcome-Aurion-](https://forums.juniper.net/t5/Engineering-Simplicity/Welcome-Aurion-to-Juniper-Networks/ba-p/295183)
1263 [to-Juniper-Networks/ba-p/295183](https://forums.juniper.net/t5/Engineering-Simplicity/Welcome-Aurion-to-Juniper-Networks/ba-p/295183), 2016. Accessed: 2018-7-9.
- 1264 239. Report, S. Santa Barbara's Aurion acquired for \$165 million. [https://www.pacbiztimes.com/2016/08/08/santa-](https://www.pacbiztimes.com/2016/08/08/santa-barbaras-aurion-acquired-for-165-million/)
1265 [barbaras-aurion-acquired-for-165-million/](https://www.pacbiztimes.com/2016/08/08/santa-barbaras-aurion-acquired-for-165-million/), 2016. Accessed: 2018-7-9.
- 1266 240. Hong, T.; Ran, G.Z.; Chen, T.; Pan, J.Q.; Chen, W.X.; Wang, Y.; Cheng, Y.B.; Liang, S.; Zhao, L.J.; Yin, L.Q.; Zhang,
1267 J.H.; Wang, W.; Qin, G.G. A Selective-Area Metal Bonding InGaAsP-Si Laser. *IEEE Photonics Technol. Lett.* **2010**,
1268 *22*, 1141–1143.
- 1269 241. Hong, T.; Li, Y.P.; Chen, W.X.; Ran, G.Z.; Qin, G.G.; Zhu, H.L.; Liang, S.; Wang, Y.; Pan, J.Q.; Wang, W. Bonding
1270 InGaAsP/ITO/Si Hybrid Laser With ITO as Cathode and Light-Coupling Material. *IEEE Photonics Technol. Lett.*
1271 **2012**, *24*, 712–714.
- 1272 242. Jhang, Y.H.; Tanabe, K.; Iwamoto, S.; Arakawa, Y. InAs/GaAs Quantum Dot Lasers on Silicon-on-Insulator Substrates
1273 by Metal-Stripe Wafer Bonding. *IEEE Photonics Technol. Lett.* **2015**, *27*, 875–878.
- 1274 243. Van Campenhout, J.; Rojo-Romeo, P.; Van Thourhout, D.; Seassal, C.; Regreny, P.; Di Cioccio, L.; Fedeli, J.M.; Baets,
1275 R. Thermal Characterization of Electrically Injected Thin-Film InGaAsP Microdisk Lasers on Si. *J. Lightwave*
1276 *Technol.* **2007**, *25*, 1543–1548.
- 1277 244. Keyvaninia, S.; Muneeb, M.; Stanković, S.; Van Veldhoven, P.J.; Van Thourhout, D.; Roelkens, G. Ultra-thin DVS-BCB
1278 adhesive bonding of III-V wafers, dies and multiple dies to a patterned silicon-on-insulator substrate. *Opt. Mater.*
1279 *Express* **2012**, *3*, 35.
- 1280 245. Wang, R.; Vasiliev, A.; Muneeb, M.; Malik, A.; Sprengel, S.; Boehm, G.; Amann, M.C.; Šimonytė, I.; Vizbaras, A.;
1281 Vizbaras, K.; Baets, R.; Roelkens, G. III-V-on-Silicon Photonic Integrated Circuits for Spectroscopic Sensing in the
1282 2-4 μm Wavelength Range. *Sensors* **2017**, *17*, 1788.

- 1283 246. Wang, Z.; Junesand, C.; Metaferia, W.; Hu, C.; Wosinski, L.; Lourdudoss, S. III-Vs on Si for photonic applications—A
1284 monolithic approach. *Mater. Sci. Eng. B* **2012**, *177*, 1551–1557.
- 1285 247. Ustinov, V.M.; Zhokov, A.E.; Zhukov, A.E.; Egorov, A.Y.; Maleev, N.A. *Quantum dot lasers*; Vol. 11, Oxford University
1286 Press on Demand, 2003.
- 1287 248. Dingle, R.; Henry, C.H. Quantum effects in heterostructure lasers, 1976. US Patent 3,982,207.
- 1288 249. Arakawa, Y.; Sakaki, H. Multidimensional quantum well laser and temperature dependence of its threshold current.
1289 *Applied Physics Letters* **1982**, *40*, 939–941.
- 1290 250. Mi, Z.; Yang, J.; Bhattacharya, P.; Qin, G.; Ma, Z. High-performance quantum dot lasers and integrated
1291 optoelectronics on Si. *Proceedings of the IEEE* **2009**, *97*, 1239–1249.
- 1292 251. Liu, G.; Stintz, A.; Li, H.; Malloy, K.; Lester, L. Extremely low room-temperature threshold current density diode
1293 lasers using InAs dots in In_{0.15}Ga_{0.85}As quantum well. *Electronics Letters* **1999**, *35*, 1163–1165.
- 1294 252. Bimberg, D.; Grundmann, M.; Ledentsov, N.N. *Quantum dot heterostructures*; John Wiley & Sons, 1999.
- 1295 253. Deppe, D.G.; Shavritranuruk, K.; Ozgur, G.; Chen, H.; Freisem, S. Quantum dot laser diode with low threshold and
1296 low internal loss. *Electronics Letters* **2009**, *45*, 54–56.
- 1297 254. Mi, Z.; Yang, J.; Bhattacharya, P.; Huffaker, D. Self-organised quantum dots as dislocation filters: the case of
1298 GaAs-based lasers on silicon. *Electronics Letters* **2006**, *42*, 1.
- 1299 255. Lee, A.D.; Jiang, Q.; Tang, M.; Zhang, Y.; Seeds, A.J.; Liu, H. InAs/GaAs quantum-dot lasers monolithically grown on
1300 Si, Ge, and Ge-on-Si substrates. *IEEE Journal of Selected Topics in Quantum Electronics* **2013**, *19*, 1901107–1901107.
- 1301 256. Chen, S.; Li, W.; Wu, J.; Jiang, Q.; Tang, M.; Shutts, S.; Elliott, S.N.; Sobiesierski, A.; Seeds, A.J.; Ross, I.; others.
1302 Electrically pumped continuous-wave III–V quantum dot lasers on silicon. *Nature Photonics* **2016**, *10*, 307.
- 1303 257. Stiens, J.; De, C.; Shkerdin, G.; Kotov, V.; Vounckx, R.; Vandermeire, W. Infrared Thermo-Electric Photodetectors. In
1304 *Laser Pulse Phenomena and Applications*; 2010.
- 1305 258. Baehr-Jones, T.; Hochberg, M.; Scherer, A. Photodetection in silicon beyond the band edge with surface states.
1306 *Opt. Express* **2008**, *16*, 1659.
- 1307 259. Knights, A.P.; Bradley, J.D.B.; Gou, S.H.; Jessop, P.E. Silicon-on-insulator waveguide photodetector with
1308 self-ion-implantation-engineered-enhanced infrared response. *J. Vac. Sci. Technol. A* **2006**, *24*, 783–786.
- 1309 260. Jayatilaka, H.; Murray, K.; Guillén-Torres, M.Á.; Caverley, M.; Hu, R.; Jaeger, N.A.E.; Chrostowski, L.; Shekhar, S.
1310 Wavelength tuning and stabilization of microring-based filters using silicon in-resonator photoconductive heaters.
1311 *Opt. Express* **2015**, *23*, 25084.
- 1312 261. Shockley, W.; Read, W.T. Statistics of the Recombinations of Holes and Electrons. *Physical Review* **1952**, *87*, 835–842.
- 1313 262. Chen, H.; Verheyen, P.; De Heyn, P.; Lepage, G.; De Coster, J.; Balakrishnan, S.; Absil, P.; Yao, W.; Shen, L.; Roelkens,
1314 G.; Van Campenhout, J. -1 V bias 67 GHz bandwidth Si-contacted germanium waveguide p-i-n photodetector for
1315 optical links at 56 Gbps and beyond. *Opt. Express* **2016**, *24*, 4622.
- 1316 263. Wang, J.; Yao, Z.; Lei, T.; Poon, A.W. Silicon coupled-resonator optical-waveguide-based biosensors using
1317 light-scattering pattern recognition with pixelized mode-field-intensity distributions. *Scientific reports* **2014**,
1318 *4*, 7528.
- 1319 264. Chao, C.Y.; Guo, L.J. Biochemical sensors based on polymer microrings with sharp asymmetrical resonance.
1320 *Applied Physics Letters* **2003**, *83*, 1527–1529.
- 1321 265. Hu, J.; Sun, X.; Agarwal, A.; Kimerling, L.C. Design guidelines for optical resonator biochemical sensors. *JOSA B*
1322 **2009**, *26*, 1032–1041.
- 1323 266. Li, H.; Liu, X.; Li, L.; Mu, X.; Genov, R.; Mason, A.J. CMOS electrochemical instrumentation for biosensor
1324 microsystems: a review. *Sensors* **2016**, *17*, 74.
- 1325 267. Li, L.; Liu, X.; Mason, A.J. Die-level photolithography and etchless parylene packaging processes for on-CMOS
1326 electrochemical biosensors. Circuits and Systems (ISCAS), 2012 IEEE International Symposium on. IEEE, 2012, pp.
1327 2401–2404.
- 1328 268. Huang, Y.; Mason, A.J. Lab-on-CMOS integration of microfluidics and electrochemical sensors. *Lab on a Chip*
1329 **2013**, *13*, 3929–3934.
- 1330 269. Datta-Chaudhuri, T.; Abshire, P.; Smela, E. Packaging commercial CMOS chips for lab on a chip integration. *Lab*
1331 *on a Chip* **2014**, *14*, 1753–1766.
- 1332 270. Laplatine, L.; Luan, E.; Cheung, K.; Ratner, D.M.; Dattner, Y.; Chrostowski, L. System-level integration of active
1333 silicon photonic biosensors using Fan-Out Wafer-Level-Packaging for low cost and multiplexed point-of-care
1334 diagnostic testing. *Sensors and Actuators B: Chemical* **2018**, *273*, 1610–1617.

- 1335 271. Li, L.; Yin, H.; Mason, A.J. Epoxy Chip-in-Carrier Integration and Screen-Printed Metalization for Multichannel
1336 Microfluidic Lab-on-CMOS Microsystems. *IEEE transactions on biomedical circuits and systems* **2018**.